REPORT DOCUMENTATION PAGE

Form Approved
OMB No. 0704-0188

1a. REPORT SECURITY CLASSIFICATION
Unclassified

1b RESTRICTIVE MARKINGS

2a. SECURITY CLASSIFICATION AUTHORITY

3 DISTRIBUTION / AVAILABILITY OF REPORT
Approved for public release; distribution is unlimited.

2b. DECLASSIFICATION / DOWNGRADING SCHEDULE

4 PERFORMING ORGANIZATION REPORT NUMBER(S)

5. MONITORING ORGANIZATION REPORT NUMBER(S)

6a. NAME OF PERFORMING ORGANIZATION
Naval Postgraduate School

6b. OFFICE SYMBOL (If applicable)
33

7a. NAME OF MONITORING ORGANIZATION
Naval Postgraduate School

6c. ADDRESS (City, State, and ZIP Code)
Monterey, CA 93943-5000

7b. ADDRESS (City, State, and ZIP Code)
Monterey, CA 93943-5000

8a. NAME OF FUNDING / SPONSORING ORGANIZATION

8b. OFFICE SYMBOL (If applicable)

9 PROCUREMENT INSTRUMENT IDENTIFICATION NUMBER

8c. ADDRESS (City, State, and ZIP Code)

10 SOURCE OF FUNDING NUMBERS

PROGRAM ELEMENT NO.	PROJECT NO.	TASK NO	WORK UNIT ACCESSION NO

11. TITLE (Include Security Classification)
EXPERIMENTAL CONSIDERATIONS OF HIGHER ORDER PARAMETRIC X-RAYS FROM SILICON CRYSTALS OF VARYING THICKNESSES

12. PERSONAL AUTHOR(S)
Evertson, Scott R.

13a. TYPE OF REPORT	13b. TIME COVERED	14. DATE OF REPORT (Year, Month, Day)	15. PAGE COUNT
Master's Thesis	FROM _____ TO _____	June 1992	72

16. SUPPLEMENTARY NOTATION
The views expressed in this thesis are those of the author and do not reflect the official policy or position of the Department of Defense or the U.S. Government.

17. COSATI CODES			18. SUBJECT TERMS (Continue on reverse if necessary and identify by block number)
FIELD	GROUP	SUB-GROUP	Parametric X-Radiation, PXR, Silicon, Linear Accelerator, Bragg Scattering, Crystalography

19. ABSTRACT (Continue on reverse if necessary and identify by block number)

Generation of parametric x-radiation (PXR) may be described as the Bragg scattering of virtual photons to produce real x-rays which satisfy the Bragg condition $n\lambda = 2d\sin\theta_B$, where θ_B is the angle between the electron beam and the crystal plane. Enhanced higher order parametric s-radiation from the <220> and the <111> planes of silicon crystals of varying thicknesses were observed. Production of PXR of order n=1 for both planes of a 20 μm thick crystal and orders n=1, and n=2 of the <220> and the n=1, n=3, and n=4 of the <111> planes of the 44 μm and 320 μm crystals were observed. Exploiting the formation and attenuation lengths of silicon crystals of varying thicknesses, higher order x-ray production is enhanced relative to the lower energy first order x-ray. Photons of 4.5 to 21 keV have been observed.

T260055

20. DISTRIBUTION / AVAILABILITY OF ABSTRACT
☒ UNCLASSIFIED/UNLIMITED ☐ SAME AS RPT. ☐ DTIC USERS

21. ABSTRACT SECURITY CLASSIFICATION
Unclassified

22a. NAME OF RESPONSIBLE INDIVIDUAL
X.K. Maruyama

22b TELEPHONE (Include Area Code)
(408) 646-2431

22c. OFFICE SYMBOL
Ph/Mx

DD Form 1473, JUN 86 *Previous editions are obsolete.*

Approved for public release; distribution is unlimited

EXPERIMENTAL CONSIDERATIONS OF HIGHER ORDER PARAMETRIC X-RAYS FROM SILICON CRYSTALS OF VARYING THICKNESSES

by

Scott R. Evertson
Lieutenant, United States Navy
B.S., United States Naval Academy,1986

Submitted in partial fulfillment
of the requirements for the degree of

MASTER OF SCIENCE IN PHYSICS

from the

NAVAL POSTGRADUATE SCHOOL
June 1992

ABSTRACT

Generation of parametric x-radiation (PXR) may be described as the Bragg scattering of virtual photons to produce real x-rays which satisfy the Bragg condition $n\lambda = 2d\sin\theta_B$, where θ_B is the angle between the electron beam and the crystal plane. Enhanced higher order parametric x-radiation from the <220> and <111> planes of silicon crystals of varying thicknesses were observed. Production of PXR of the order n=1 for both planes of a 20 μm thick crystal and of the orders n=1, and n=2 of the <220> and the n=1, n=3, and n=4 of the <111> planes of a 44 μm and 320 μm crystal were observed. Exploiting the formation and attenuation lengths of silicon crystals of various thicknesses, higher order x-radiation production is enhanced relative to the lower energy first order x-ray. Photons of 4.5 to 21 keV have been observed.

E825
c.1

TABLE OF CONTENTS

I. INTRODUCTION.....1

II. THEORETICAL BACKGROUND.....2

III. PXR EXPERIMENT.....9

A. EXPERIMENT DESCRIPTION.....9

B. ENERGY CALIBRATION PROCEDURE.....11

C. PXR DATA COLLECTION.....27

D. PXR ANALYSIS.....30

1. Intensity Analysis.....37

2. Resolution Analysis.....52

IV. CONCLUSIONS AND RECOMMENDATIONS.....61

LIST OF REFERENCES.....64

INITIAL DISTRIBUTION LIST.....66

I. INTRODUCTION

The need for a monochromatic and intense x-radiation source has led to the study of the interaction of relativistic charged particles in various media. Parametric x-radiation (PXR) is a possible source.[Ref. 1] PXR is formed by a relativistic charged particle, an electron in this case, interacting with the planes of a crystalline structure at or near the Bragg condition. Ter-Mikaelian first theorized this phenomenon for the number of x-rays produced in a thin crystal[Ref. 2]. In 1985, Baryshevsky et al conducted the first experiment at Tomsk to observe PXR. 900 MeV electrons bombarded a diamond crystal at a Bragg angle of 45 degrees producing parametric x-rays in the 5 to 25 keV range.[Ref. 3]

The Naval Postgraduate School (NPS) experiment was the first measurement of PXR in the United States. The PXR source crystal for the experiment described in this thesis was silicon.

The measurements in this thesis demonstrate how the enhancement of higher order PXR due to the x-ray formation and attenuation in silicon were affected by the crystal thickness. This thesis continues the investigation started in Reference 4.

II. THEORETICAL BACKGROUND

Parametric x-radiation is one of several methods for producing x-rays when a charged particle beam interacts with a crystal. Other production methods include transition, diffraction, and channeling radiation. Comparison of the various x-ray sources has shown PXR gives the highest spectral intensity.[Ref. 5]

When a charged particle beam satisfies the Bragg condition with the crystal lattice, the virtual photons associated with the relativistic particles are diffracted. PXR is produced when the periodic electric susceptibility associated with the crystal lattice structure interacts with the field of the particles.[Ref. 2]

The periodic arrangement of atoms in a crystal leads to the diffraction of x-ray photons with the wave vector $\mathbf{k}$ which satisfies the Bragg condition

$$k^2 = (\mathbf{k}_0 + \tau)^2, \qquad |\mathbf{k}| = |\mathbf{k}_0|, \tag{1}$$

where τ is the reciprocal lattice vector and $\mathbf{k}_0$ is the wave vector of the incoming virtual photons. This process is illustrated in Figure 1. In the x-ray range, the refractive index $n(\mathbf{k},\omega)$ becomes greater than unity and the Vavilov-Cherenkov radiation requirement,

$$1 - \frac{\mathbf{k} \cdot \mathbf{v}}{\omega} n(\mathbf{k}, \omega) = 0, \qquad \hbar = c = 1, \qquad (2)$$

is fulfilled even though the dielectric constant is less than one. PXR originates when both the Bragg and Vavilov-Cherenkov conditions are satisfied by the wave vector $\mathbf{k}$ and the frequency ω of the photons generated by the charged particles moving through the lattice structure of a crystal with uniform velocity.[Ref. 3] In contrast to the crystal structure, homogeneous media require that the refractive index n be less than one for the production of x-rays, thus

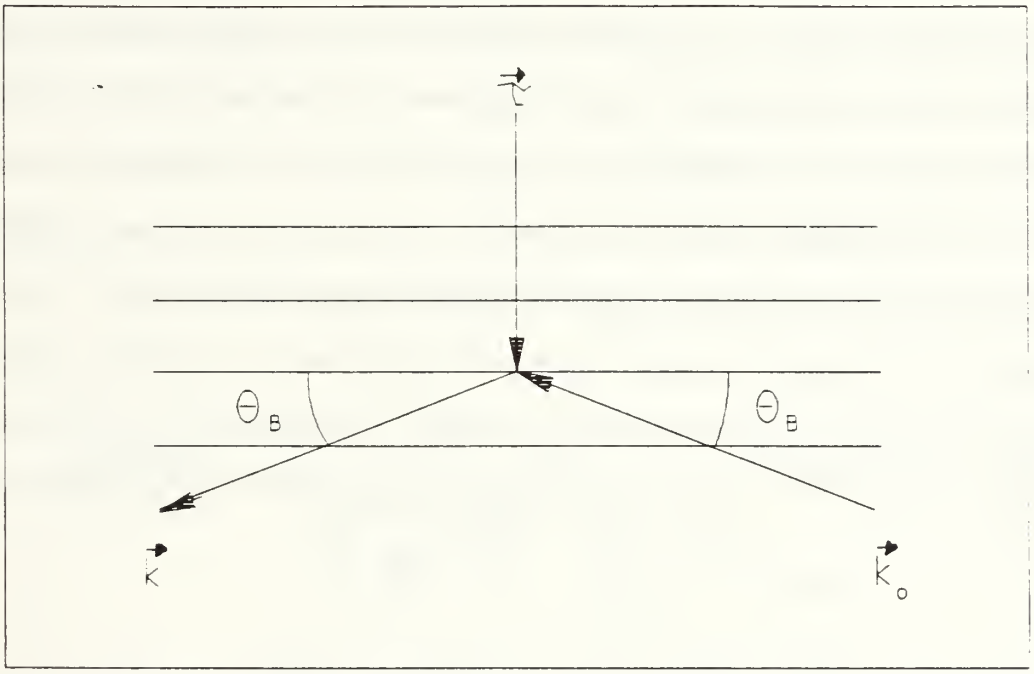

Figure 1. Diffraction of virtual photons associated with a relativistic charged particle by the planes of a crystal [Ref. 2].

demonstrating that under the Bragg diffraction condition the Vavilov-Cherenkov radiation is PXR.

Kinematic theory of PXR is applicable for real crystals, which consist of thin mosaic blocks turned relative to each other at the angle $\delta = m/E$. Here m is the mass of the particle in the beam and E is the energy of the particle in the beam. Ter-Mikaelian formulated the expression for the number of photons emitted by a charged particle in a thin crystal; treating the interaction as a perturbation with the crystal requirement

$$kL|n-1| < 1, \tag{3}$$

where L is the thickness of the crystal. If the refraction of photons and the multiple scattering of electrons in the crystal are accounted for, then the results, for a mosaic crystal with $\delta > m/E$ and with PXR from different blocks being incoherent, remain correct. The spectral and angular distributions of emitted photons are formulated by

$$\frac{\partial^2 N}{\partial \mathbf{n}_\perp \partial \omega} = \frac{e^2}{2\pi}\omega L_a |g_r|^2 \frac{\left|\mathbf{k}_\perp, \frac{\omega}{v^2}\mathbf{v} + \boldsymbol{\tau}\right|^2}{\left[\left(\mathbf{k}_\perp - \boldsymbol{\tau}_\perp\right)^2 + \frac{\omega^2}{v^2}\left(1 - v^2\right)\right]^2}\left[1 - e^{(-L/L_a)}\right]\delta(q), \tag{4}$$

$$q = \frac{\omega}{v} - \sqrt{\omega^2 - \mathbf{k}^2} + \tau_z - \frac{\omega}{2}\left[\mathrm{Re}(g_0) - \theta_s^2\right], \tag{5}$$

$$\theta_s = \frac{E_s}{E}\sqrt{\frac{L}{L_R}}. \tag{6}$$

The Fourier components $|g_\tau|$ of the dielectric susceptibility corresponding to the reciprocal lattice vector and the mean value g_0 are directly related by the coherent scattering amplitude of the photons. θ_s is the angle of multiple scattering, $E_s \equiv 21$ MeV, and L_R is the radiation length. Equation (4) is written in a coordinate system with the z-axis directed along the particle velocity $\mathbf{v}$; $\mathbf{k}_\perp = \omega \mathbf{n}_\perp$; and $La = [\omega Im(g_0)]^{-1}$. [Ref. 5]

The characteristic of producing quasimonochromatic photons at large angles relative to the velocity vector, $\mathbf{v}$, distinguishes PXR from other radiation mechanisms. The particle energy does not determine the emitted photons wave vectors, $\mathbf{k}$, nor frequencies ω_B. The photons are defined by the reciprocal lattice vector, τ, and the Bragg angle, θ_B, between $\mathbf{v}$ and the crystallographic planes associated with τ. The PXR maxima are defined by the crystal lattice structure amplitudes corresponding to τ. The values of the emitted wave vectors, $\mathbf{k}$, and frequencies ω_B are

$$\mathbf{k} = \frac{\omega_B \mathbf{v}}{v^2} + \tau; \qquad \frac{\mathbf{k} \cdot \mathbf{v}}{\omega_B} = \cos 2\theta_B, \tag{7}$$

$$\omega_B(n) = \frac{\tau^2}{2|\tau_z|} = \frac{\tau}{2 \sin\theta_B} = \frac{n\pi c}{d \sin\theta_B}, \qquad n=1,2,3... \tag{8}$$

where d is the distance between the crystal planes corresponding to the vector τ. [Ref. 3]

The intensity of PXR is proportional to $|g_\tau|^2$ and therefore it is greater in crystals with higher packing factors, such as a diamond lattice. Rotation of a crystal by some $\Delta\theta$ results in the emitted wave vector, $\mathbf{k}$, rotating $2\Delta\theta$ in the same direction while the frequency varies as a result of equation (8). The angular distribution of emitted photons can be derived by integrating equation (4) over ω, resulting in

$$\frac{\partial^2 N}{\partial\theta_x \partial\theta_y} = \sum_{n=1}^{\infty} \frac{e^2}{4\pi}\omega_B L_a\left[1 - e^{-L/L_a}\right] \frac{\left|g_\tau(\omega_B(n))\right|^2}{\sin^2\theta_B} \frac{\left[\theta_x^2 \cos^2 2\theta_B + \theta_y^2\right]}{\left[\theta_x^2 + \theta_y^2 + \theta_{ph}^2\right]}; \quad (9)$$

$$\theta_{x,y} = \frac{(\mathbf{k_0} - \mathbf{k})_{x,y}}{\omega_B}; \qquad \theta_{ph}^2 = \frac{m^2}{E^2} + \theta_s - |g_0|, \quad (10)$$

where m is the rest mass of the electron.

The frequency distribution can be determined by integrating equation (4) over $\mathbf{n}_\perp$, resulting in

$$\frac{\partial N}{\partial u} = N_1 J_1(u);$$

$$J_1(u) = \frac{1 + u^2\left(1 + \cos^2 2\theta_B\right)}{\left(1 + u^2\right)^{3/2}}; \quad (11)$$

$$N_1 = \frac{\pi}{2} N_0; \qquad u = \frac{\sin\theta_B}{\cos\theta_B} \frac{(\omega - \omega_B)}{\omega_B \theta_{ph}}.$$

The number of photons detected in an angular distribution of θ_D about θ_B is given by

$$N_D = \pi N_0 \left(1 + \cos^2 \theta_B\right) \int_0^{\rho_D} \frac{\rho^3}{\left(\rho^2 + 1\right)} d\rho \qquad (12)$$

$$= N_1 \left(1 + \cos^2 2\theta_B\right) \ln\left[\frac{\theta_D^2 + \theta_{ph}^2}{\theta_{ph}^2} - \frac{\theta_D^2}{\theta_D^2 + \theta_{ph}^2}\right],$$

where

$$\rho_D = \frac{\theta_D}{\theta_{ph}}. \qquad (13)$$

The detector angular size is a factor in determining the value of N_D, even for $\theta_D >> \theta_{ph}$. This factor does not occur in channeling or in bremsstrahlung radiation; however in PXR, the intensity slowly decreases as θ^{-1} away from the Bragg condition angle.

The angular distribution as defined by the parameter $\theta_{ph}(E)$ increases for the electron energy

$$E < E_{opt} = \sqrt{\frac{m^2 + E_s^2 \frac{L}{L_R}}{\left|Re(g_o)\right|}}, \qquad (14)$$

thus setting the limiting threshold energy for PXR. The amount of photons decreases rapidly for $E < E_{opt}$. The number detected becomes

$$N_D = \frac{\pi}{2} N_0 (1 + \cos^2 2\theta_B) \frac{1}{2} \left(\frac{\theta_D}{\theta_{ph}} \right)^4 \approx \left(\frac{E}{E_{opt}} \right)^4 . \qquad (15)$$

This phenomena illustrates the problem that--even if all other parameters are met--if the beam energy is not sufficient PXR may not be observed.[Ref. 5]

Reference 4 was used extensively for the presentation of the derivation given above.

III. PXR EXPERIMENT

The dependence of parametric x-ray generation on crystal thickness was studied using silicon crystals with thicknesses of 20 μm, 44 μm, and 320 μm. Two specific properties were examined; first, how was the PXR intensity effected by the crystal thickness, second, how did the PXR linewidth change as a function of x-ray photon energy.

A. EXPERIMENT DESCRIPTION

The NPS Linear Accelerator (LINAC) was used to conduct this experiment. Since the LINAC is pulsed at 60 Hz with a pulsewidth of one microsecond, the low duty factor required the measurements be made with only dark current, estimated to be much lower than a nanoampere average current. The electron beam energy was 85 MeV.

The experimental set-up is pictured in Figure 2. It consisted of a scattering chamber with a target support ladder (holding the silicon crystal) in the vacuum chamber center. An alignment/reference laser was located outside the vacuum chamber 90 degrees counter-clockwise from the incoming particle beam inlet. Attached to a chamber port 45 degrees clockwise from the beam exit port was a brass pipe fitted with a one mil Kapton window (1" in diameter) at the

end immediately before the Si(Li) x-ray detector. The detector is an EG&G ORTEC system, model number 7113-16250.

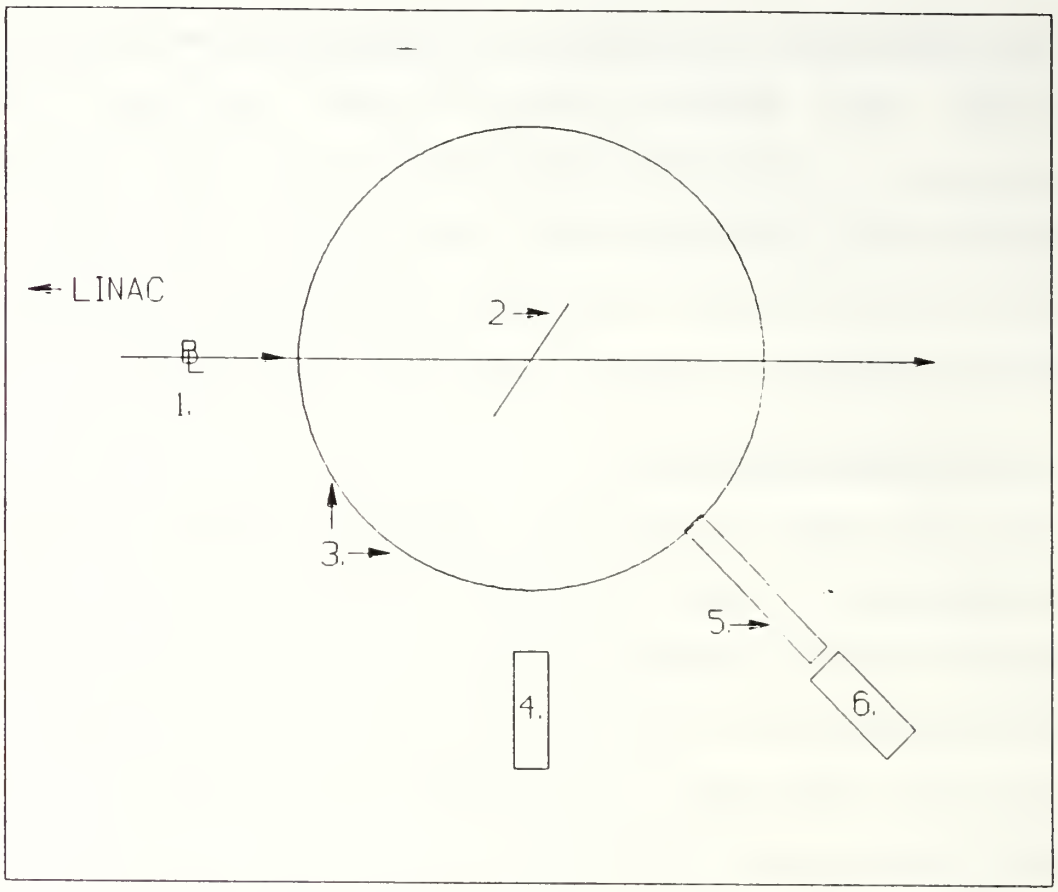

Figure 2. End station PXR experimental set-up. 1.Incoming electron beam. 2.Target ladder with silicon crystal and calibration foils. 3.Scattering chamber. 4. Reference/Alignment laser. 5. Vacuum coupled flange. 6. Si(Li) x-ray detector.

Located on the target ladder was a silicon crystal. The spacing ,d, of the <111> planes is 3.135 angstroms while the spacing of the <220> planes is 1.920 angstroms. Silicon has a density of 2.33 grams per cubic centimeter. For the experiment two separate crystals were used. The first was etched to a thickness of 20 μm in a one square centimeter

square in the center of the crystal. The second crystal was etched to 44 μm in a one square centimeter square at the center. The thickness of the area outside the center of the latter crystal was 320 μm. The tolerance in the thickness measurements were unknown, and the thickness uncertainties were assumed to be negligible for the main conclusions of this study.

θ_C is the angle between the alignment laser and the back surface of the crystal and is used for positioning the appropriate planes of the crystal at the Bragg condition angle, θ_B. The laser defined the zero or home position. The incoming beam entered the scattering chamber through the 270° port. The Bragg angle, θ_B, was referenced to the electron beam. as indicated by Figure 3. The Bragg angle for this experiment was 22.5°, with the detector located at an angle of $\theta_D = 2\theta_B$.

B. ENERGY CALIBRATION PROCEDURE

To calibrate the parametric x-ray energy, a calibration target consisting of stacked Cu and Ti foils that was overlayed on the backside of a phosphorescent screen. Figure 4 is a drawing of this device.

PXR must be detected during the on-time of the electron beam pulse. Consequently, the detector and its associated electronics exist in an environment which is affected by the klystron RF noise and ground loops. Measurements of x-rays

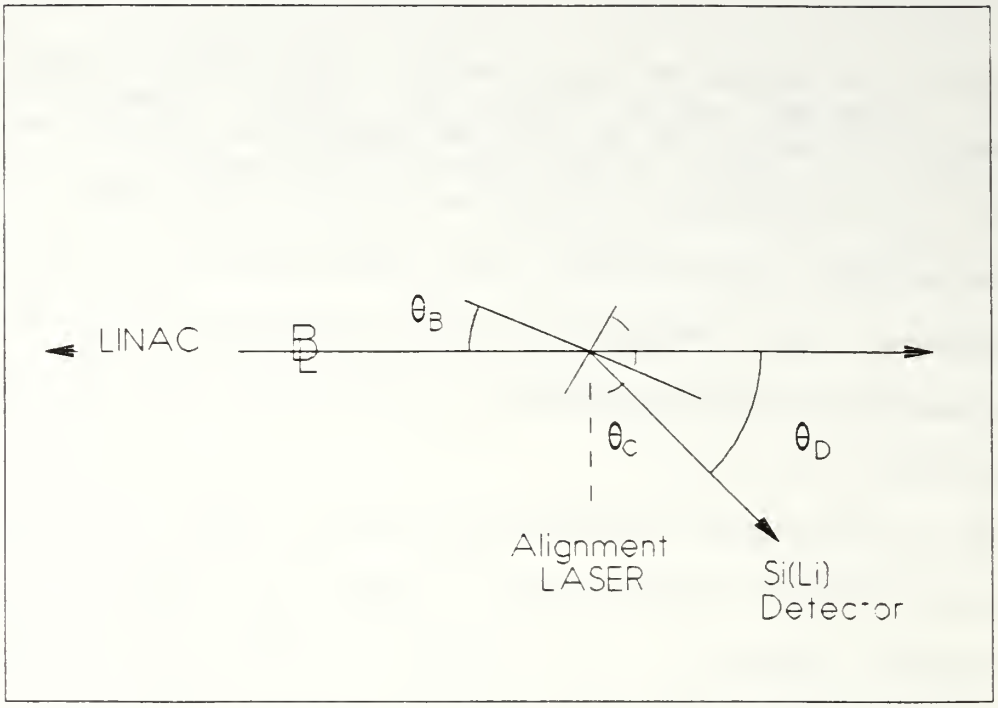

Figure 3. This picture depicts the relationship between the incoming charged particle beam and the crystal planes and the angle, θ_C, between the alignment laser and the crystal's back surface. The detector angle, θ_D, is twice the Bragg angle, θ_B.

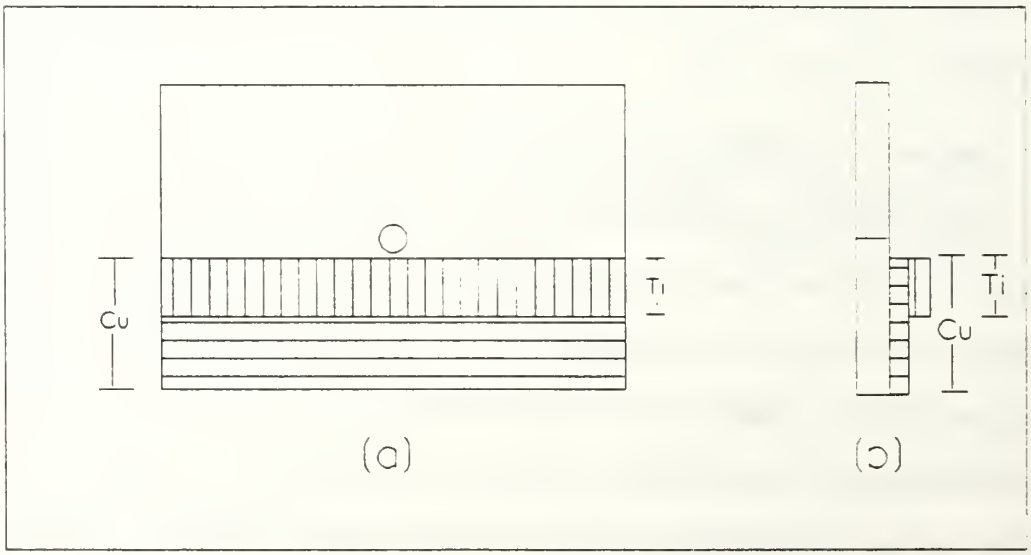

Figure 4. The drawings indicate how the calibration foils were placed on the phosphorescent screen. (a). is the backside of the screen. (b) is the left edge of the screen.

during the beam pulse are affected by the noise environment and will appear at apparent energies which do not correspond to the calibration from standard sources taken when the beam was off. Consequently a technique had to be devised to energy calibrate the spectrum during the machine on-time. During the course of this experiment a method was developed to calibrate the detector using x-ray floresence.

The procedure required that the Cu and Ti foils be placed in the path of the incoming electron beam. De-excitation K-edge x-rays following the interactions of the electrons in the beam with the atoms in the foils were observed. The x-rays that reached the Si(Li) detector were counted at a rate of one photon per machine pulse. (The accelerator pulse at a rate of 60 Hz with a pulse duration of one microsecond.)

With a spectrum of titanium and copper K_α peaks--signal to noise ratio on the order of 10 to 1--the resolution of the detector could be approximated. The resolution of the detector could then be applied to the PXR spectra.

The K_α x-ray peak of titanium should be observed at 4.5 keV while that of copper should be seen at 8.05 keV [Ref. 6]. Figure 5 is a plot of the calibration spectrum taken July 22, 1991. In it, the signal to noise ratio for both the titanium and the copper peaks is approximately 10:1. Additionally, the K_α and the K_β lines were resolved at 8.05

keV and 8.94 keV respectively. On September 05, 1991, another calibration spectrum was made (Fig. 6). Here the signal to noise ratio of titanium was approximately 3:1, while that of the copper was closer to 2:1[1]. During the PXR experiment, only the Ti and Cu calibration lines were obtained. In order to obtain a calibration line for all the peaks observed, a subsequent measurement of the fluorescent x-ray from titanium, copper, yttrium and indium was made. These are shown in Figures 7 thru 10. Figure 11 is a composite spectrum created from the data of Figures 7 to 10. This spectrum allows for calibrations of detector spectrum energy and width for the full range of x-rays from 5 to 30 keV. A follow-on thesis will develop a sandwich foil which will allow simultaneous measurements of all fluorescent lines in this energy range. The K_α x-ray peaks for yttrium and indium are 14.920keV and 24.104keV respectively while the K_β peaks are at 16.87 keV and 27.57 keV [Ref. 6]. With the x-ray energy peaks from the last set of de-excitation data, the detector resolution could be determined.

To determine the detector resolution, the calibration peaks were assumed to be Gaussian in shape. Next the natural linewidths of the foils had to be determined. Using

[1]The resolution of the titanium peaks is approximately the same when uncertainties are neglected.

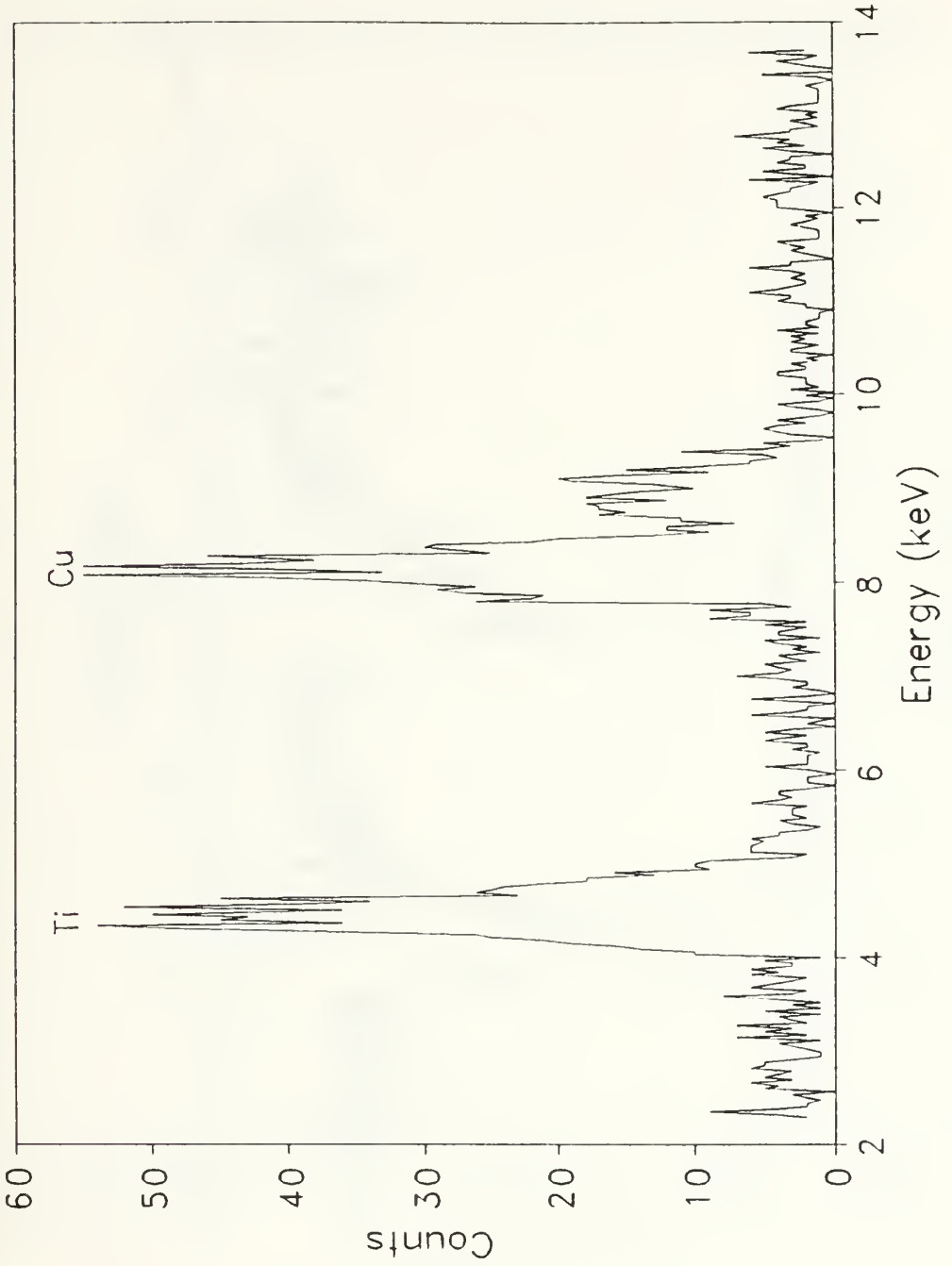

Figure 5. Calibration spectrum taken on July 22, 1991, using Ti and Cu foils in dark current.

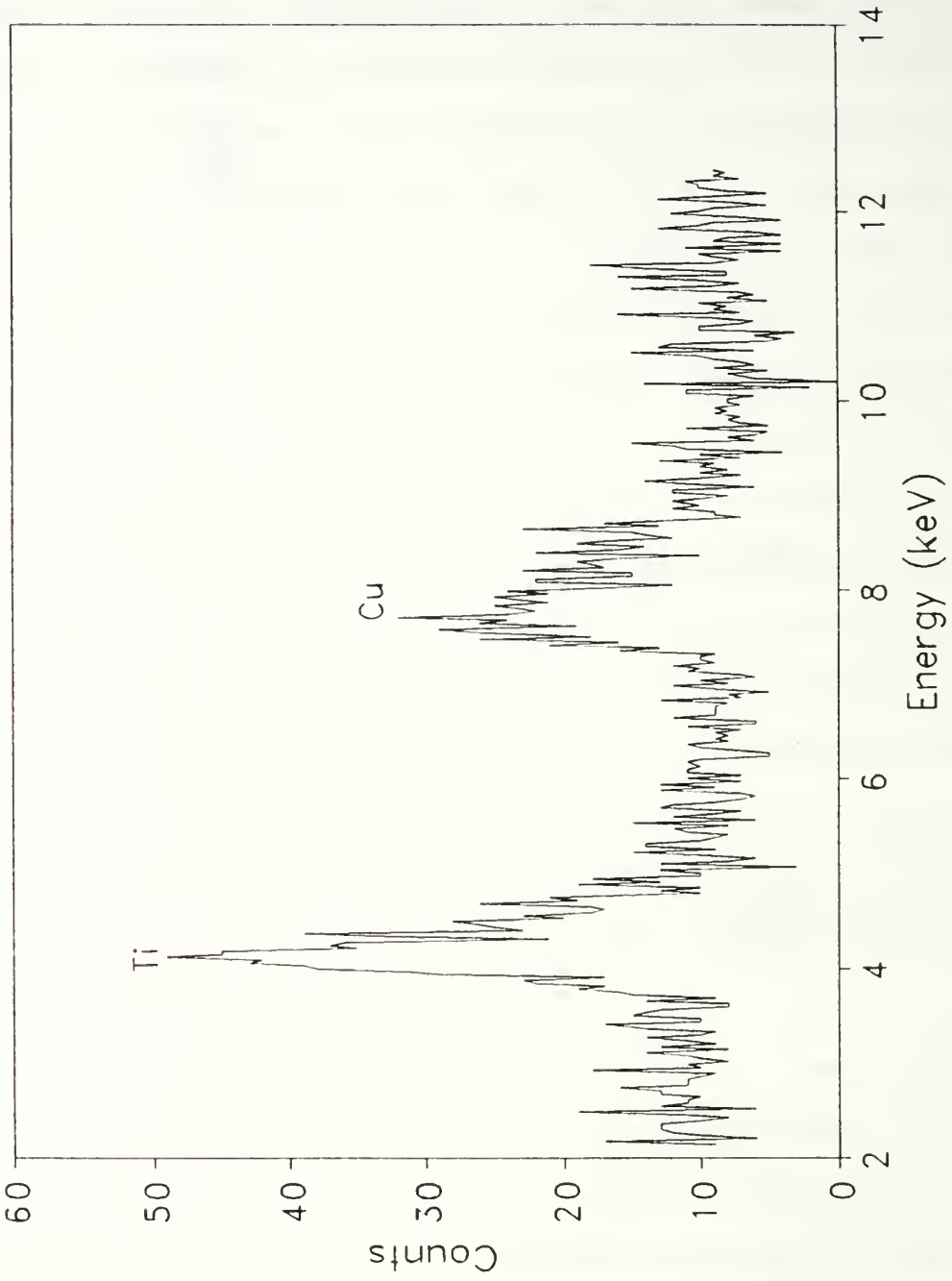

Figure 6. Calibration spectrum taken on September 05, 1991, with Ti and Cu foils in dark current.

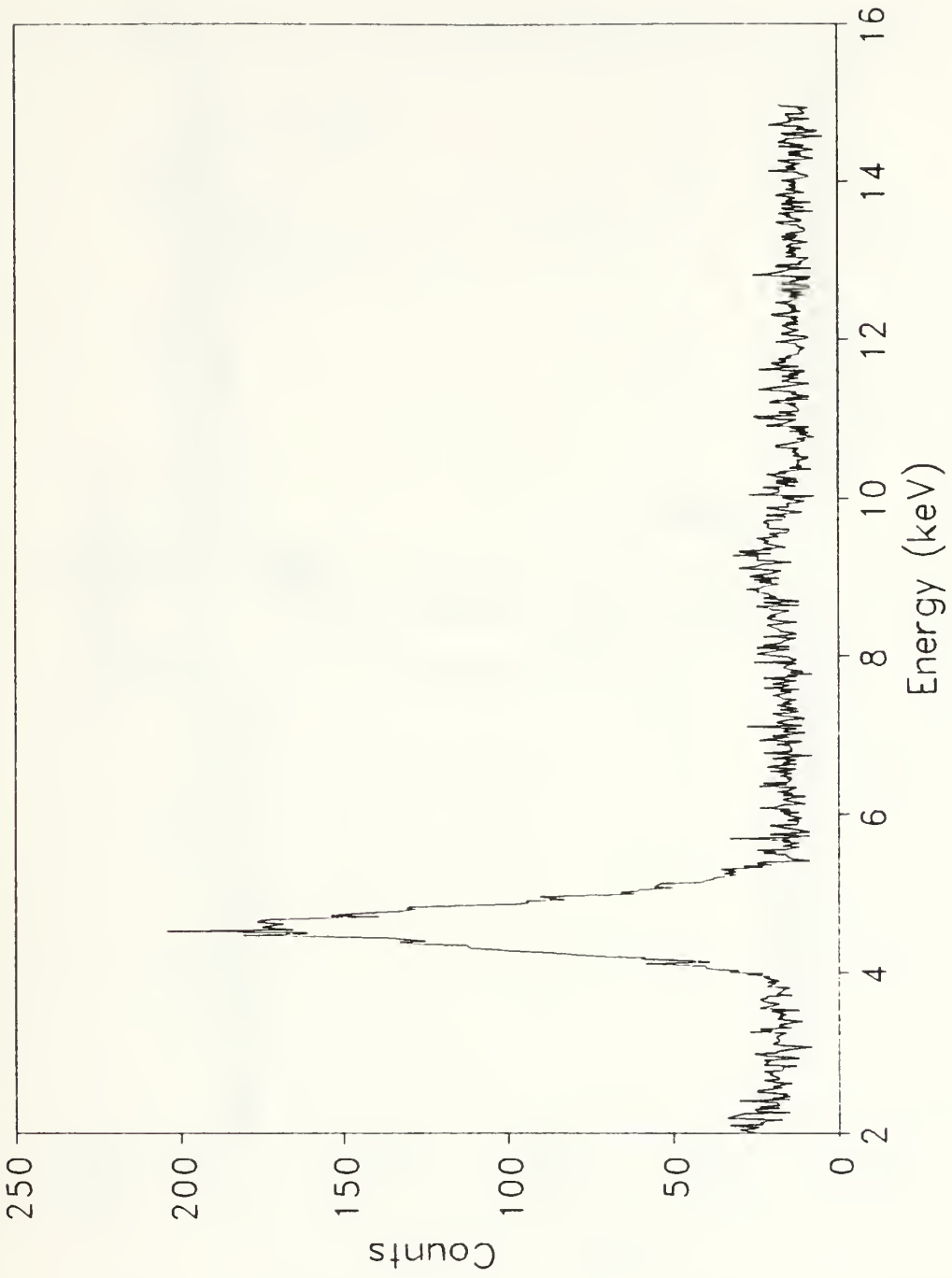

Figure 7. Calibration spectrum taken April 30, 1992, of Ti foil in dark current.

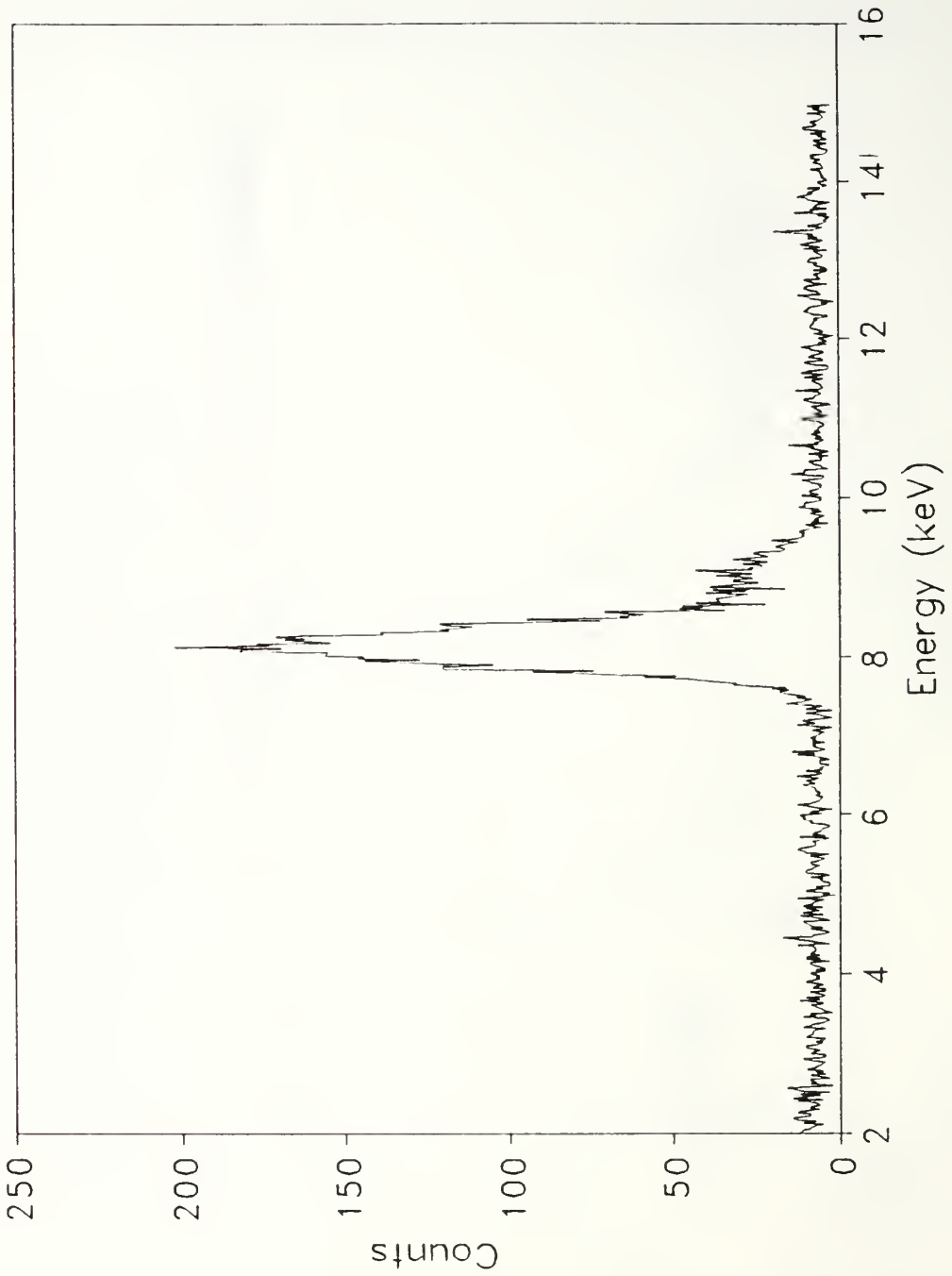

Figure 8. Calibration spectrum taken April 30, 1992, of Cu foil in dark current.

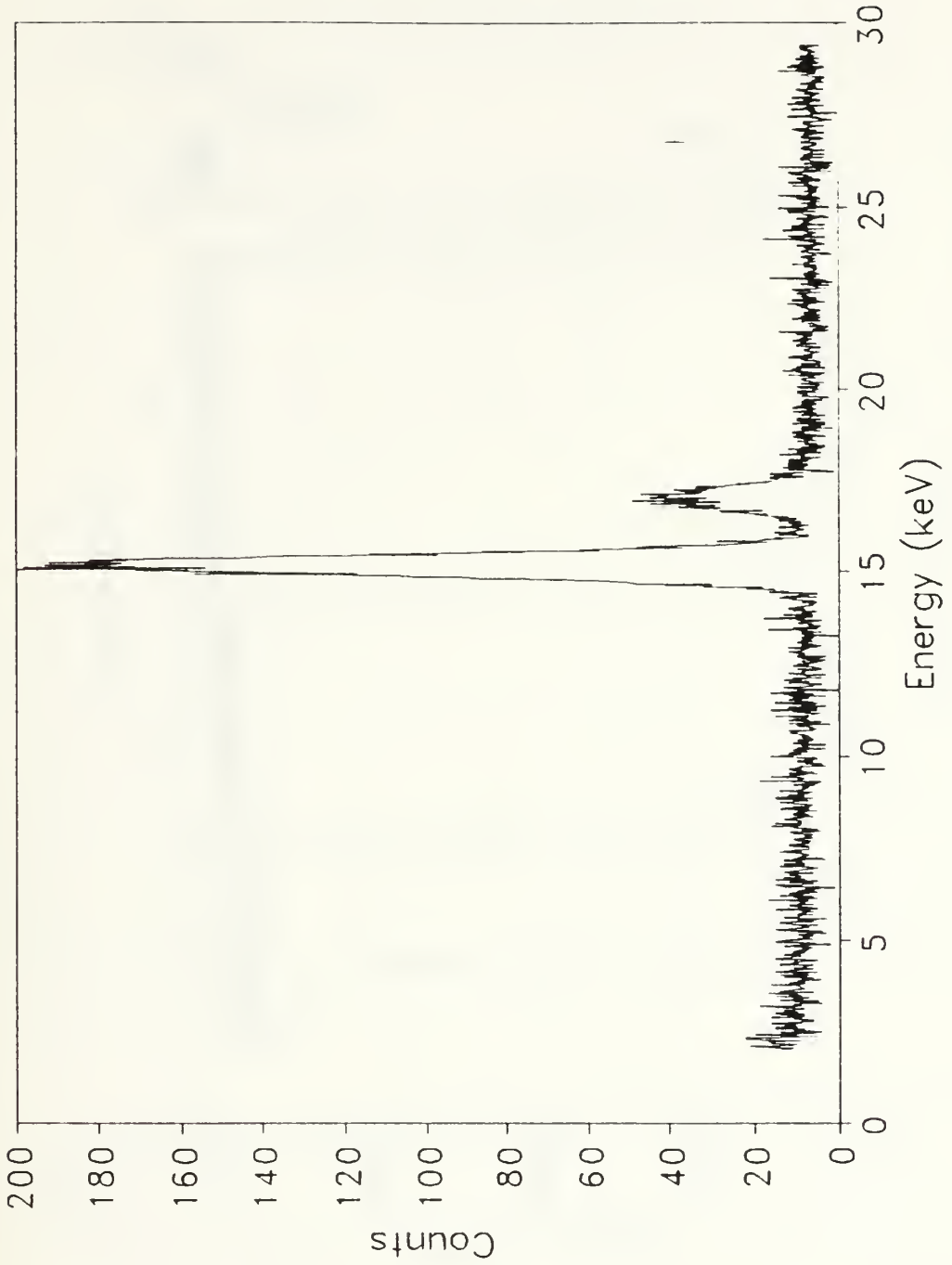

Figure 9. Calibration spectrum taken April 30, 1992, of Y, foil in dark current.

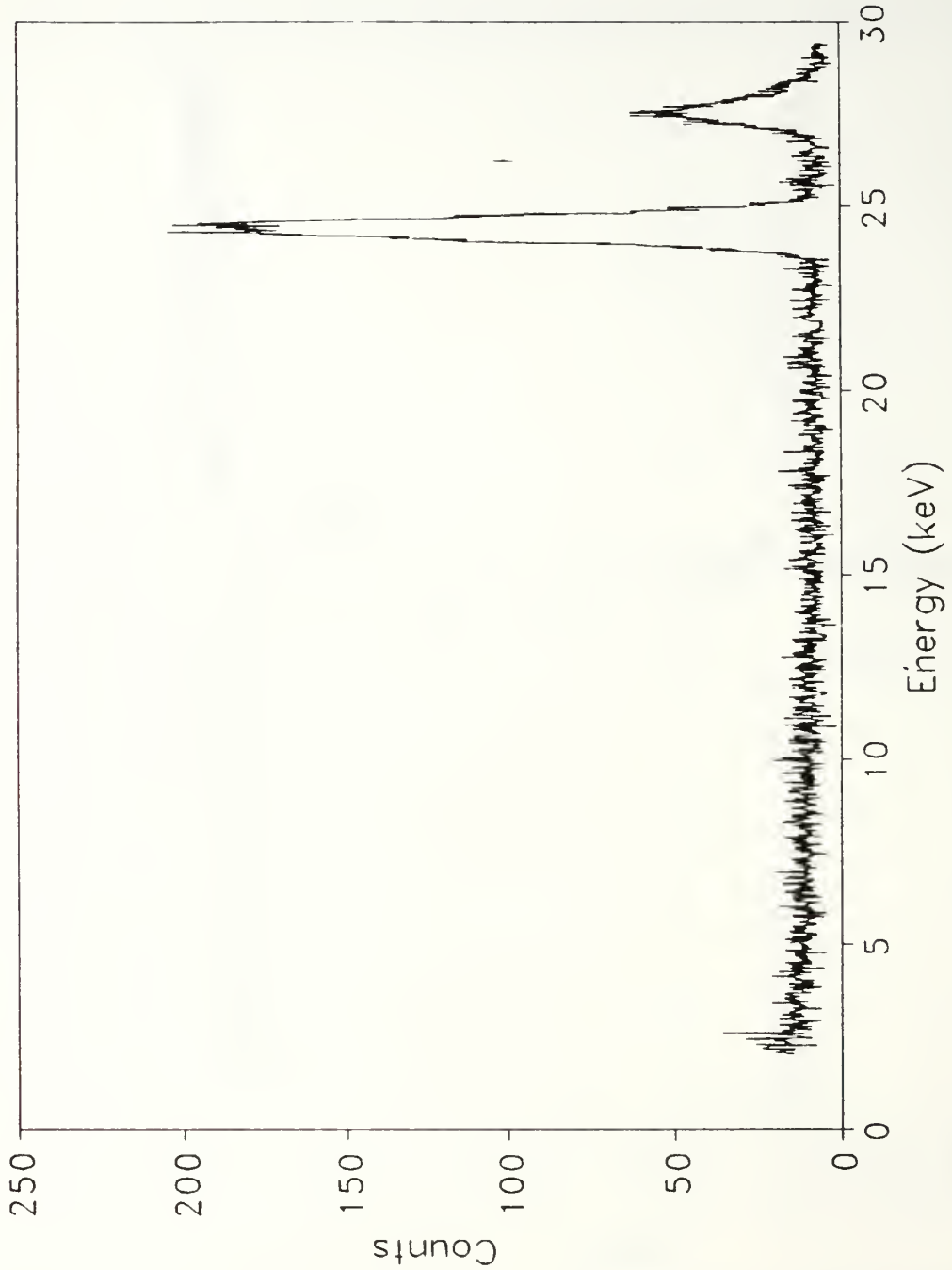

Figure 10. Calibration spectrum taken April 30, 1992, of In foil in dark current.

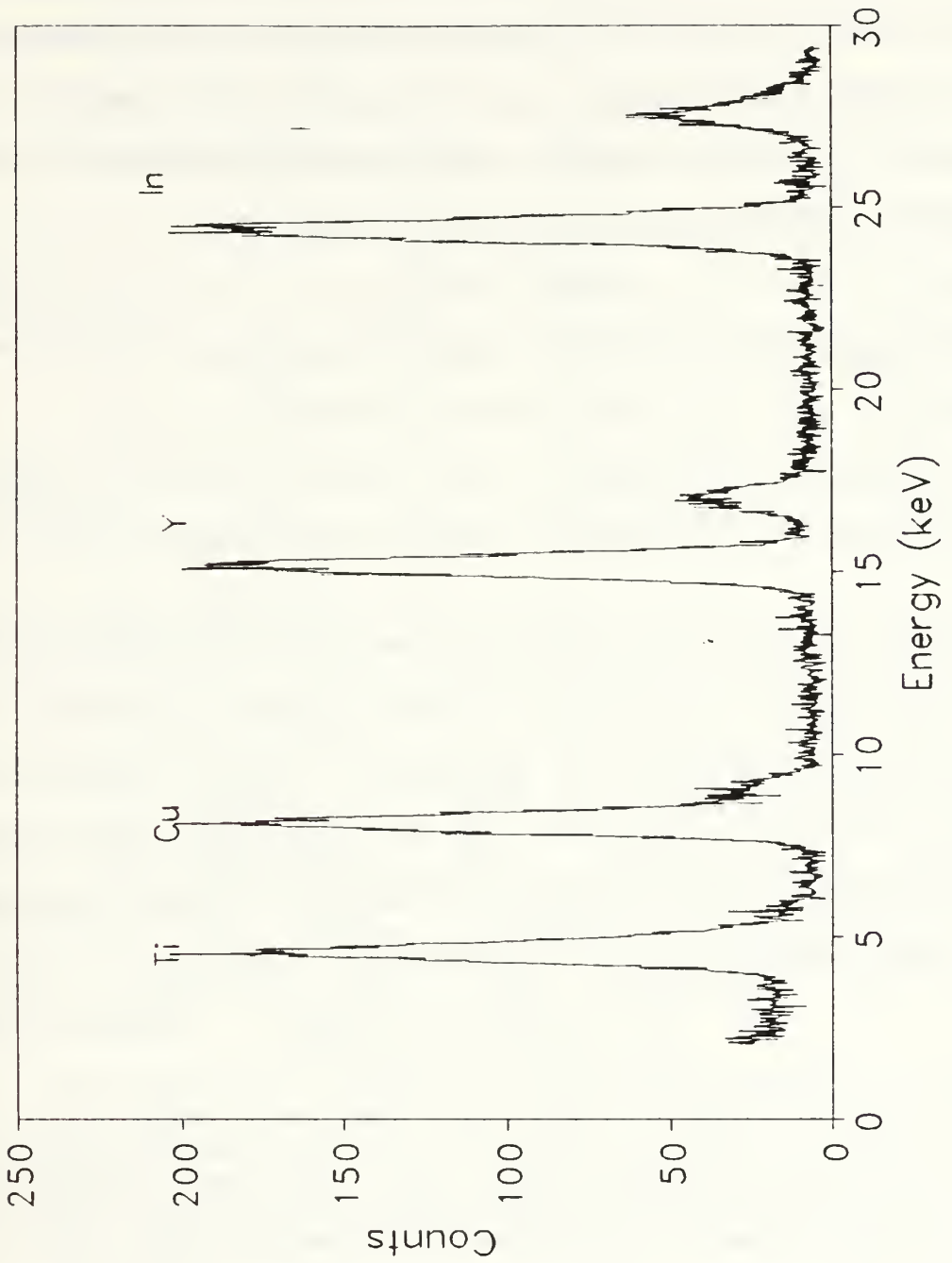

Figure 11. Composite calibration spectrum taken from April 30, 1992, Ti, Cu, Y, and In foils data (Figures 7 to 10).

Reference 7, the natural linewidths varied in size from 10 eV to 45 eV. The natural linewidths were also assumed to be Gaussian distributions. As both peaks were assumed to be Gaussian in nature, the observed linewidth is related to the detector resolution and natural linewidth by

$$\Gamma_{obs}^2 = \Gamma_{det}^2 + \Gamma_{lw}^2 \qquad (16)$$

where Γ_{obs} is the measured resolution, Γ_{det} is the detector resolution and Γ_{lw} is the natural linewidth.

Since the uncertainty in Γ_{lw} is assumed to be negligible, the uncertainty in Γ_{det} is the same as that for Γ_{obs}.

Table 1 lists the values of the K_α x-ray energy peaks, the foil natural linewidths and the observed linewidths[2] for the July 22, and April 30, spectrums. Table 2 contains the results of using equation (16) to calculate the detector linewidth. Also in Table 2 is a listing of the theoretical detector resolution as determined from

$$\Gamma_{det} = \sqrt{(\Gamma_n)^2 + (2.35\sqrt{\varepsilon F E})^2}, \qquad (17)$$

where Γ_n = 110 ev, ε =3.8 ev, F, the Fano Factor is 0.125, and E is the x-ray energy [Ref. 10]. Note the manufacturers theoretical values do not agree with measurements. Thus the value of the detector resolution to be used will be that of the observed calibration spectrum linewidths.

[2]Three independent methods were used to determine these values. They included using Personal Computer Analyzer (PCA) software [Ref. 8], spreadsheet software [Ref. 9], and measuring the linewidths by hand.

Figure 12 is a plot of the detector resolution versus peak energy for the calibrations done on July 22, and April

Date	Element	Energy (keV)	Γ_{lw} (keV)	Γ_{obs}[3] (keV)	Γ_{obs}[4] (kev)	Γ_{obs}[5] (keV)
22Jul91	Ti ($K\alpha$)	4.51	.01	.402	.4±.3	.44±.07
	Cu ($K\alpha$)	8.05	.016	.504	.48±.2	.63±.07
	Cu ($K\beta$)	8.94	*	*	*	*
30Apr92	Ti ($K\alpha$)	4.51	.01	.587	.52±.05	.54±.07
	Cu ($K\alpha$)	8.05	.016	.585	.62±.05	.60±.07
	Cu ($K\beta$)	8.94	*	*	*	*
	Y ($K\alpha$)	14.92	.0356	.633	.58±.04	.62±.07
	Y ($K\beta$)	16.87	*	*	*	*
	In ($K\alpha$)	24.10	.0437	.724	.76±.05	.70±.07
	In ($K\beta$)	27.57	*	*	*	*

Table 1. List of the calibration foils, the respective x-ray energy peak values. Included in the list are the natural linewidths of the foils and the observed linewidth values determined from PHA, spreadsheet, and hand measurements.

30. Of particular interest is the differrence in the two titanium widths and the two copper widths. Due to this difference and the lack of reference energy peaks in the 15

---

[3][Ref. 8].
[4]Hand Measurements.
[5][Ref. 9].
[6]The linewidth of Y wasn't listed in Reference 7,. The value was approximated by using the values of Sr and Zr which was .035 for both.
[7]The linewidth of In was not listed in Reference 7, but was approximated from Pd and Ag which are both at .043.

keV and 25 keV region in the July 22, data, a least squares fit was applied to the April 30, spectrum to determine the

Date	Element	Energy (keV)	Γ_{det}[8] (keV)	Γ_{det}[9] (keV)	Γ_{det}[10] (keV)	Γ_{det} (keV)
22Jul91	Ti	4.51	.402	.4±.3	.44±.07	.154
	Cu	8.04	.504	.48±.2	.63±.07	.182
30Apr92	Ti	4.51	.587	.52±.05	.54±.07	.154
	Cu	8.04	.585	.62±.05	.60±.07	.182
	Y	14.92	.632	.58±.04	.62±.07	.226
	In	24.10	.723	.75±.05	.70±.07	.274

Table 2. List of the detector resolution as determined by PCA, spreadsheet, and hand measurements. The last column represents the calculated resolution from Reference 10.

slope. The resolution as a function of photon energy was assumed to be linear. The linear regression was done using an HP15C hand held calculator. The slope was m = 0.0068 with an intercept of b = 0.543 keV and a correlation r = 0.978. Next, the value of the slope was used to plot a line to best approximate a straight line fit of the July 22, data. Figure 13 is a plot of the 22 July, data and the manufacturer's theoretical values from Table 2. Note that the manufacturer's data plots as nearly a straight line. The slope is m = 0.006, the intercept is b = 0.131 keV, and

[8][Ref. 8].
[9]Hand Measurement
[10][Ref. 9].

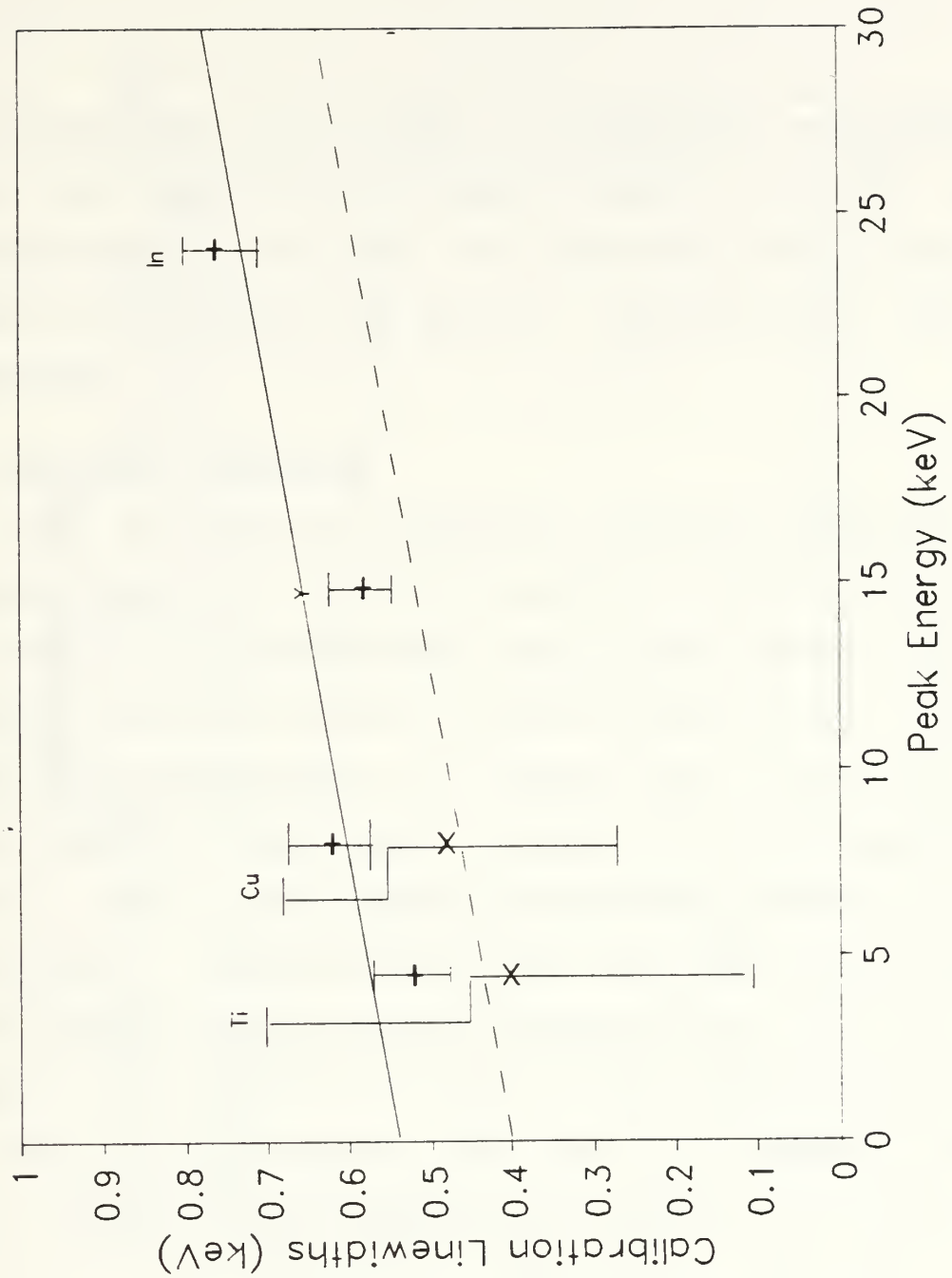

Figure 12. The plot depicts detector resolution versus foil peak energy for the calibration foils. × represents the July data while + represents the April data. The linear regression is depicted by a solid line and the transposed line used for translation of the PXR data is represented by the dashed line.

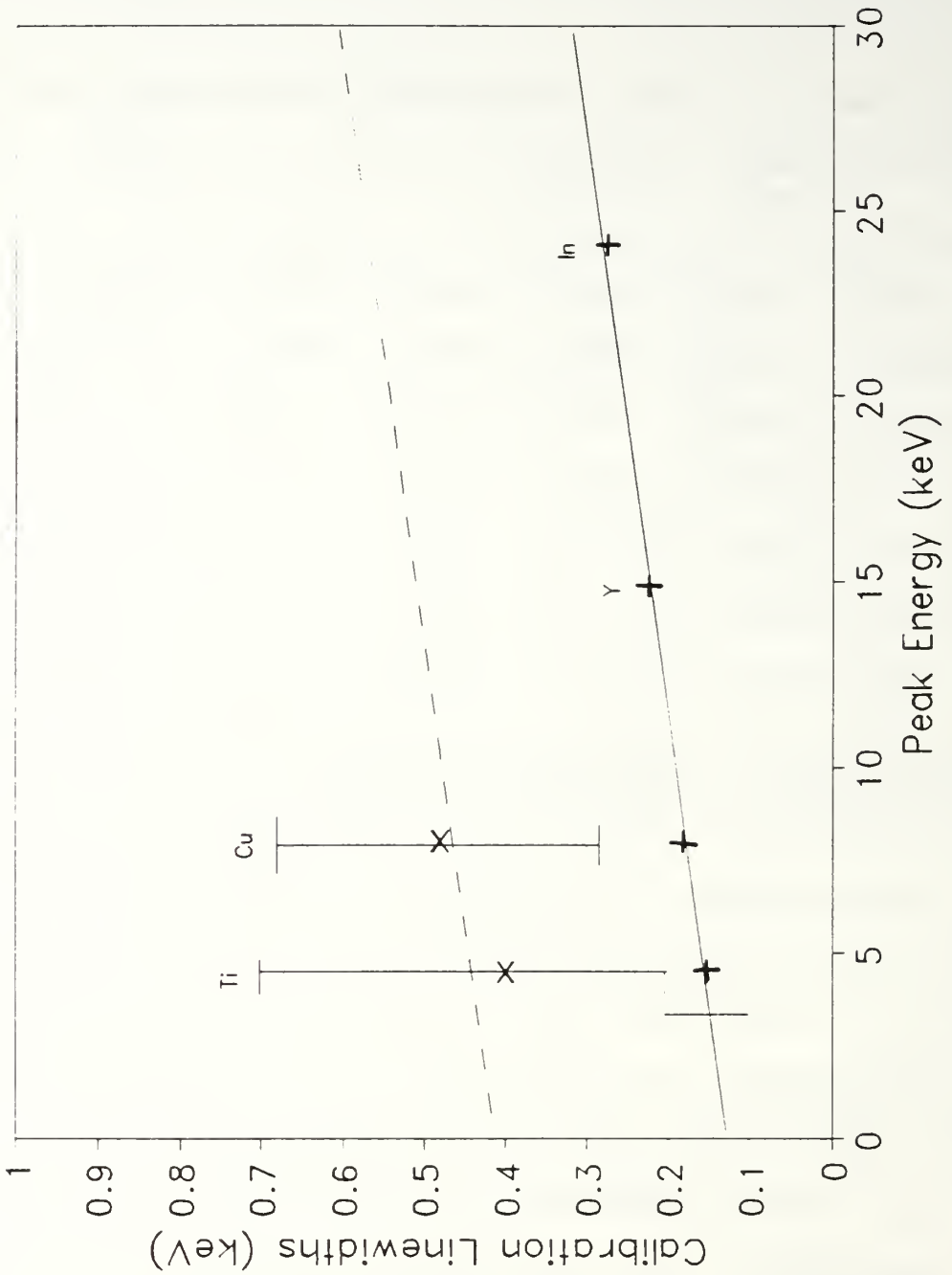

Figure 13. The plot depicts detector resolution versus foil peak energy for the calibration foils. × represents the July data while + represents the manufacturer's data. The linear regression is depicted by a solid line and a translated line used used to approximate a straght line fit to the data is represented by the dashed line.

the correlation is r = 0.9967. Consequently, the assumption that the resolution increases linearly as x-ray energy increases is valid. Thus, the transposed line in Figure 12 would then define the detector resolution for the PXR spectrums.

C. PXR DATA COLLECTION

With the initial calibration spectrum completed, the target ladder was lowered to a position such that the center of the 20 μm silicon crystal was aligned for the incoming electron beam. The ladder was then rotated to θ_c = 67.5°[11]. This angle corresponded to a Bragg angle of 22.5° for the <220> planes of the crystal. A single peak corresponding to the n=1 peak at an energy of 8.63keV was observed as shown in Figure 14. Following this run, the ladder was rotated to the reference point and then rotated to θ_c = 102.75°. In this position, the <111> planes of the crystal were aligned at the 22.5° Bragg angle. This result is plotted in Figure 15. The n=1 peak was observed at 5.19 keV.

[11]The silicon crystals were provided by Adelphi Technology Inc., and were etched so the <220> plane was perpendicular to the incoming electron beam when θ_c = 0°

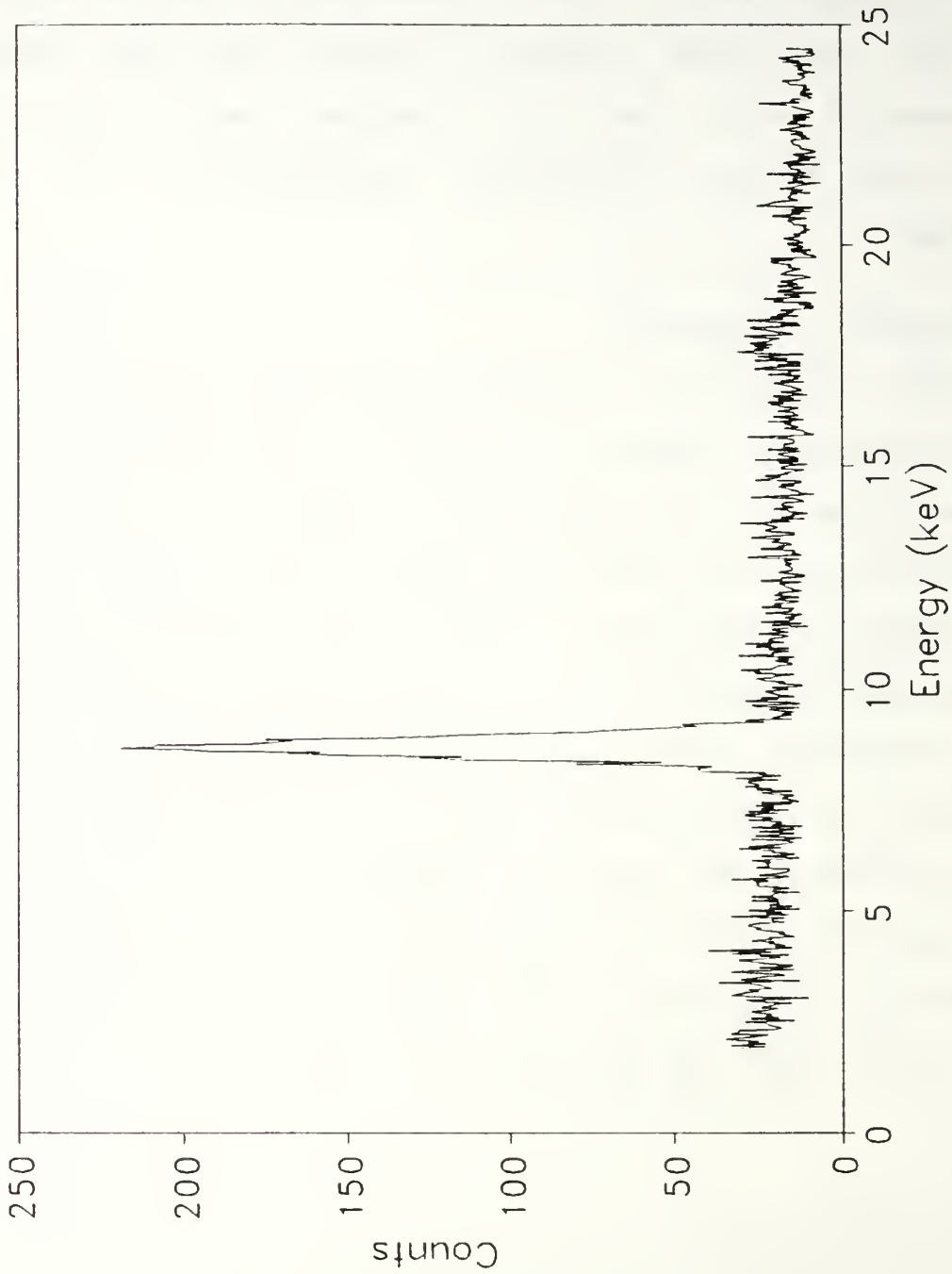

Figure 14. The plot is the n=1 peak of the 20 μm Si <220> orientation using an 85 MeV dark current electron beam. The peak is located at 8.63 keV.

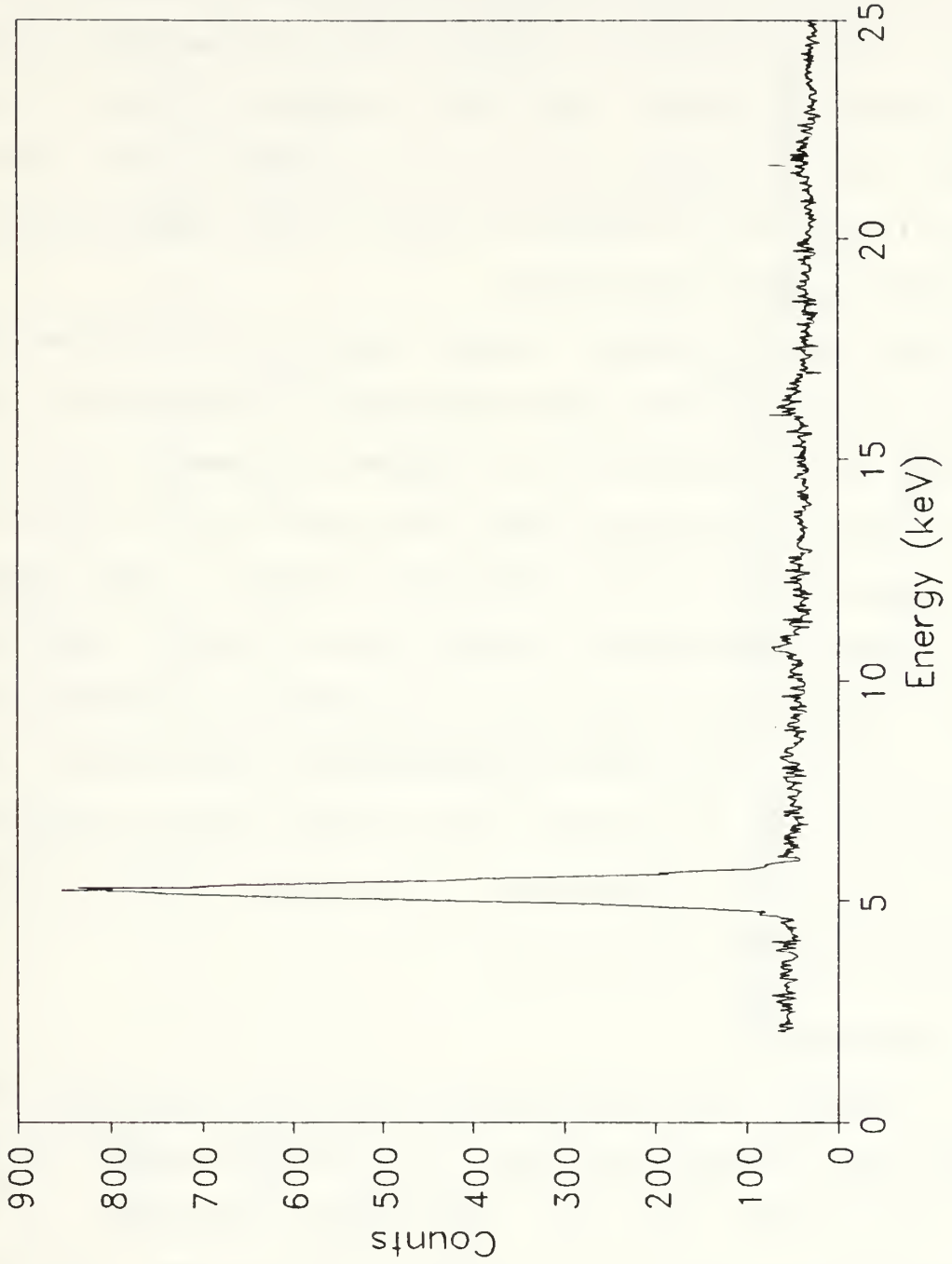

Figure 15. The n=1 peak of the 20 μm Si <111> orientation produced by an 85 Mev dark current electron beam is presented here. The peak enrgy is 5.19 keV.

The experiment was repeated with thicker crystals of 44 μm and 320 μm thickness. Figures 16-19 are the plots of the data collection runs. The data in Figures 16 and 17 was taken with the crystal rotated to an angle of θ_C =68.5°, while the data for Figures 18 and 19 was taken with the crystal rotated to θ_C =104.8°.

The target rotation angles used were obtained for maximum count rate and were determined by stepping the 44μm portion of the crystal in 0.5 degree increments from 66.5° to 70° (<220> reflection plane) and from 101.6° to 104.8° in 0.2 degree steps (<111> reflection planes). The highest count rates (photons per second) were found at 68.5° and 104.8° respectivly. This would correspond to a Bragg angle, θ_B of 21.5° and 20.46° respectively. The count rate associated with each angle was 0.06 for <220> orientation and 0.06 <111> orientation. The angle of the Si(Li) detector remained fixed at 45°.

D. PXR ANALYSIS

To analyze the PXR data that had been collected, three independent methods were used. The first required the use the PCA software [Ref. 8]. The analysis included: 1) the determination of the gross area or total number of counts under the peak, 2) the number of background counts in the region of interest, 3) the gross peak height,

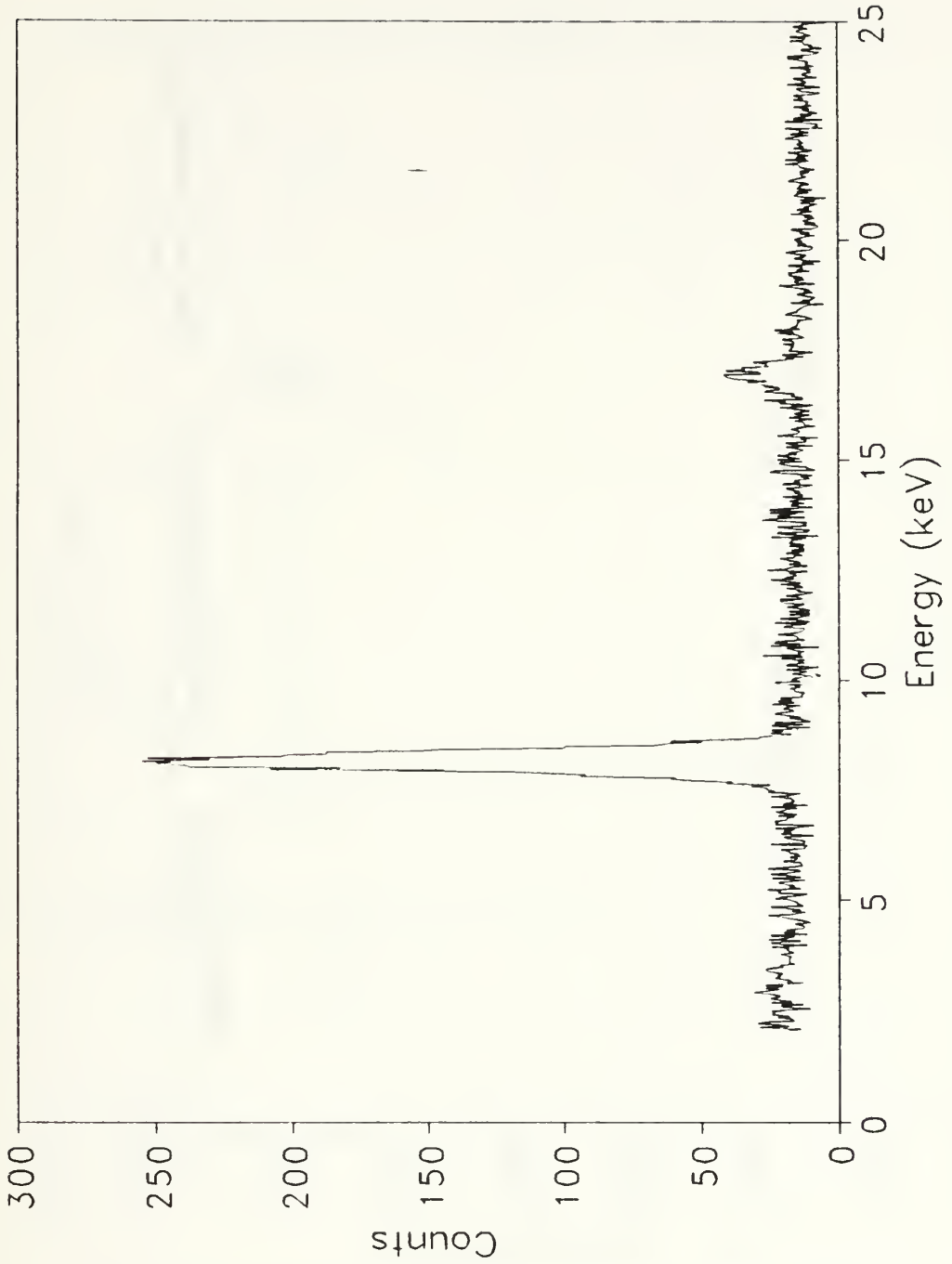

Figure 16. This plot was produced using the 44 μm Si <220> crystal orientation. The n=1 and n=2 peaks were observed at 8.17 keV and 16.97 keV respectively.

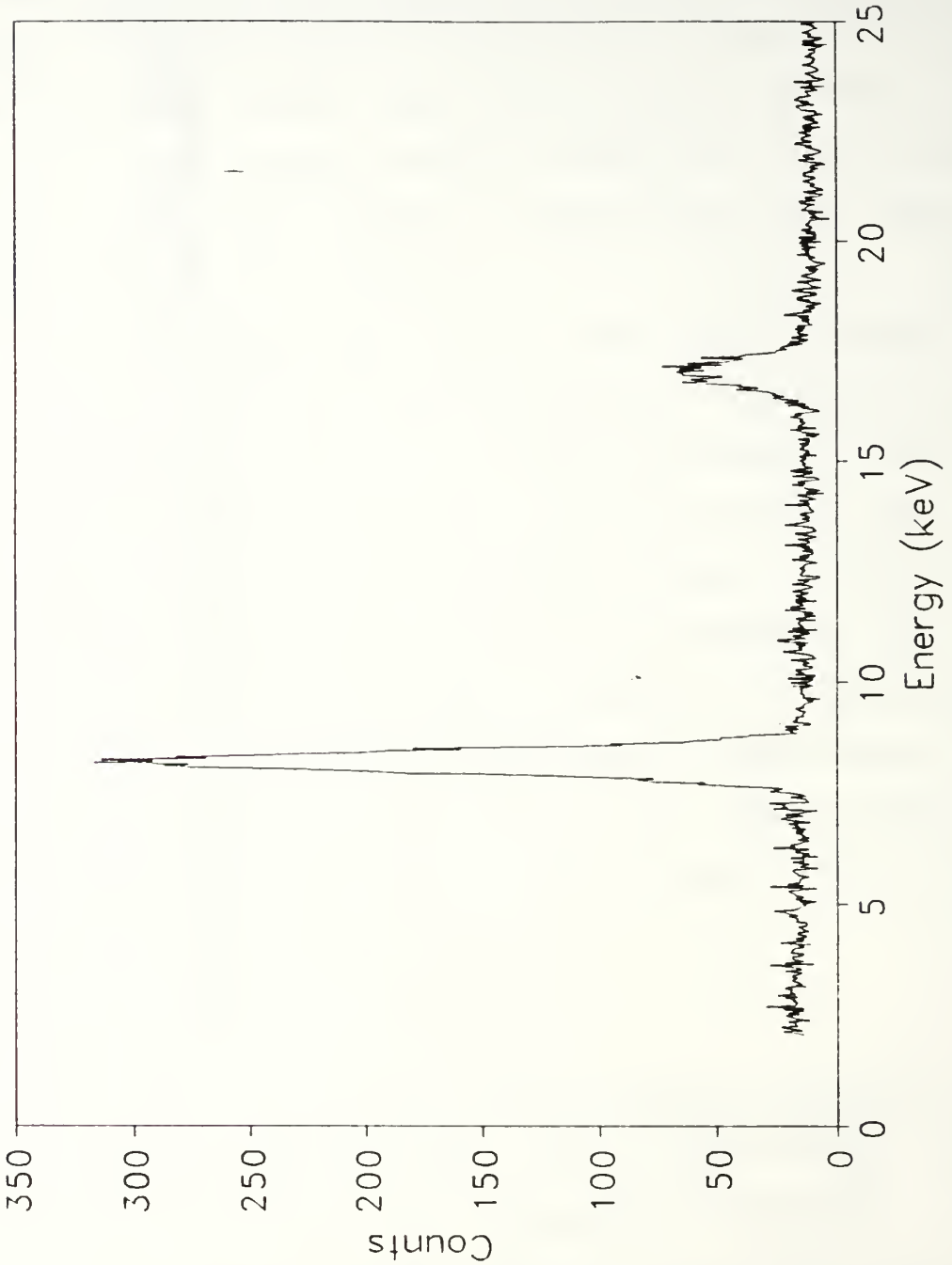

Figure 17. This plot was produced using the 320 μm Si <220> crystal orientation. The n=1 and n=2 peaks were observed at 8.21 keV and 17.16 keV respectively.

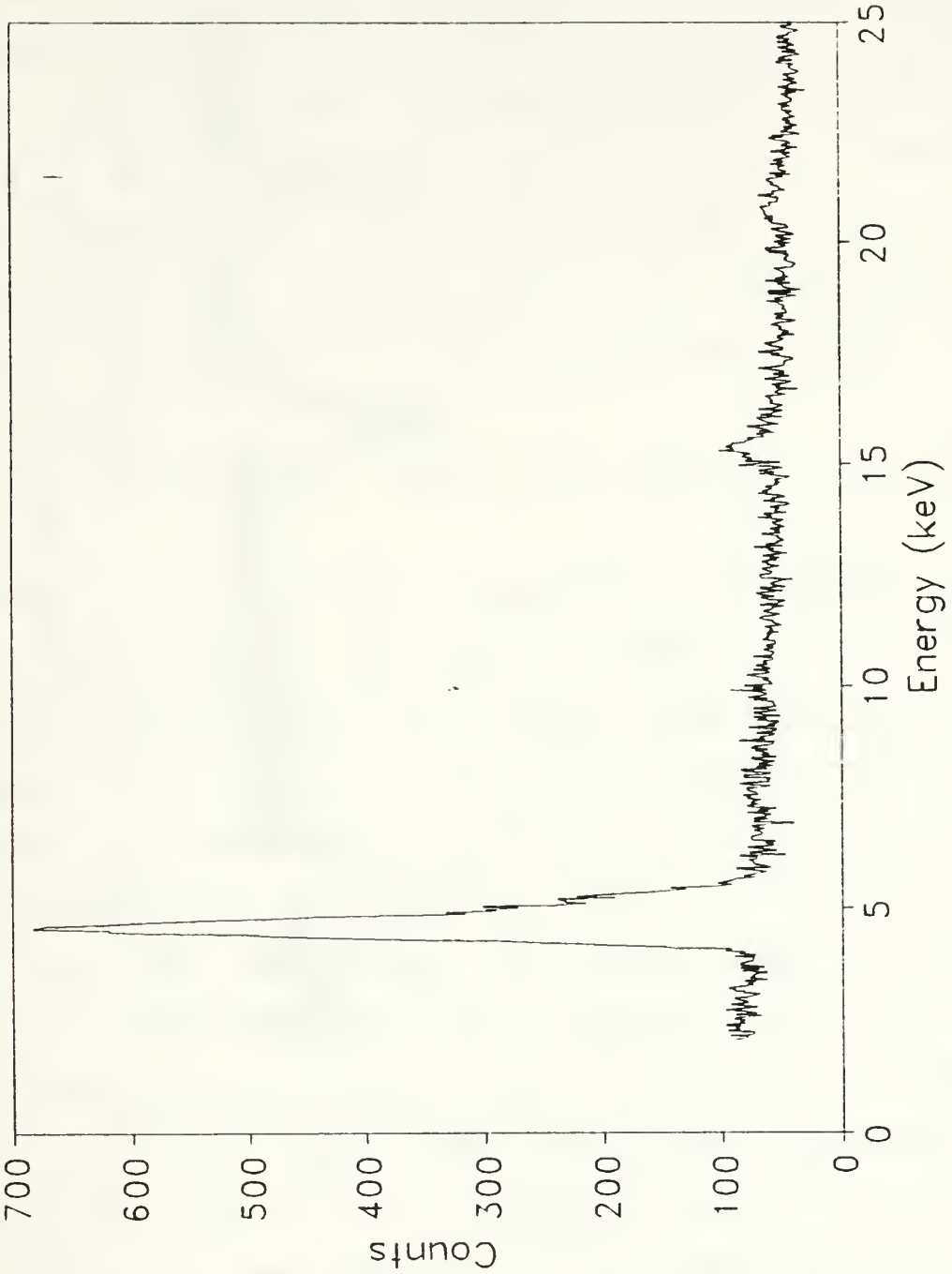

Figure 18. This plot was produced using the 44 μm Si <111> crystal orientation. The n=1,n=3, and n=4 peaks were observed at 4.56 keV, 15.31 keV, and 20.80 keV respectively.

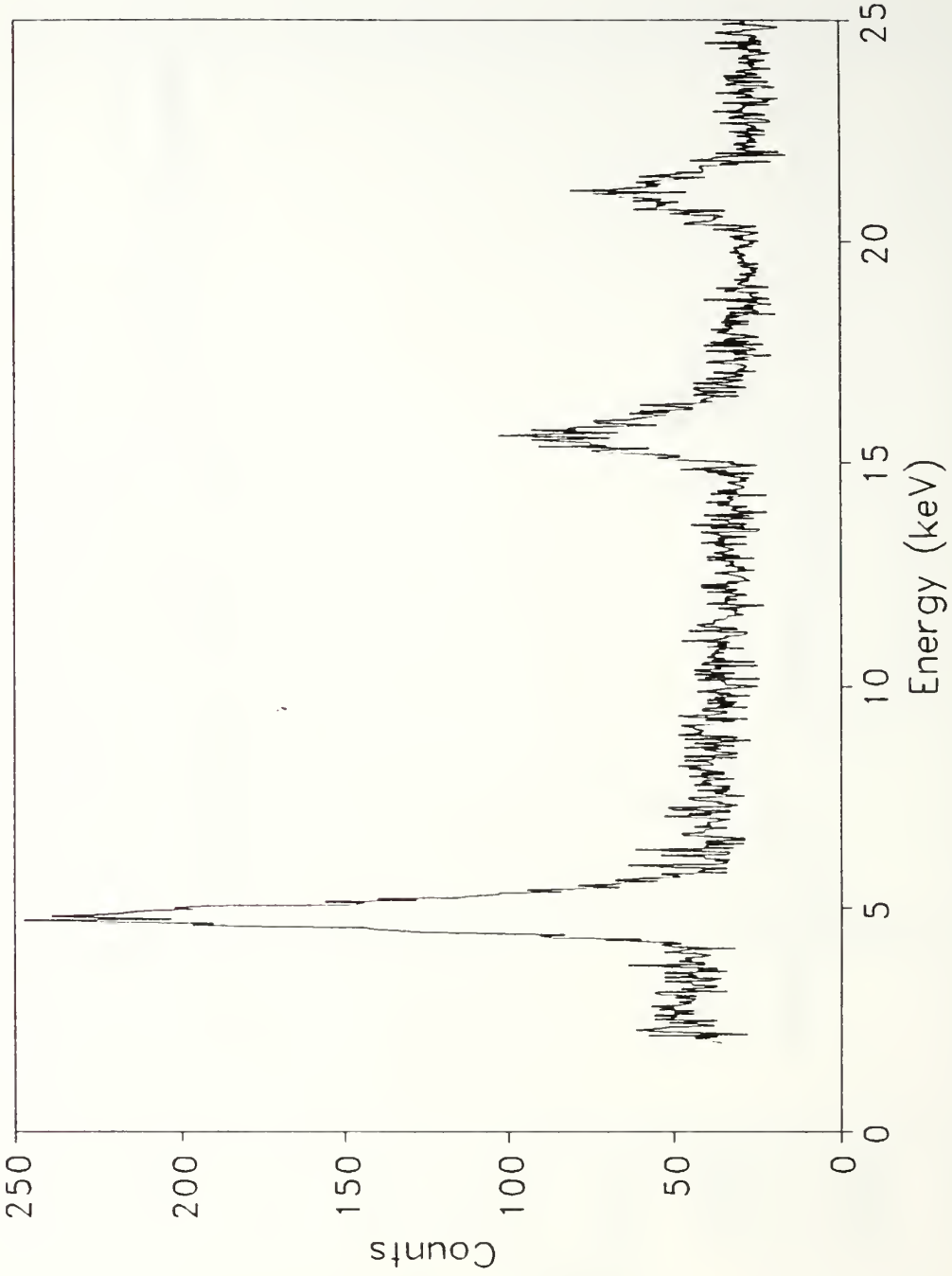

Figure 19. This plot was produced using the 320 μm Si <111> crystal orientation. The n=1, n=3, and n=4 peaks were observed at 4.72 keV, 15.62 keV, and 21.15 keV respectively.

4) the peak FWHM, and 5) the centroid of the peak. For the software to provide this information, the region of interest (ROI) had to be defined. To define the region of interest, the peak was identified and then the leading and trailing edges were estimated. PCA software provided a fast way to return some initial values; however, the uncertainties in how the background was computed has left some question as to the accuracy of the results.

The second method required the use of a spreadsheet [Ref. 9].

Before the data could be analyzed on the spreadsheet it had to be converted from binary to ASCII code. A program titled Convert written by Dr. George Rothbart was used. The program was provided by Dr. M. A. Piestrup of Adelphi Technologies Inc. With the data in ASCII format it was imported into the spreadsheet software.

Using the spreadsheet, the areas--gross, net, and background--were computed. The observed resolution was also determined. As with the PCA software a region of interest was defined for each x-ray peak. The procedure for determining the ROI was different from that done using Reference 8. The background for the spectrum had to be determined. In the case of the <220> orientation spectras, the average background was a constant across the spectrum. For the <111> orientation a straight line was fit to

approximate the non-zero slope of the background. Once the background had been computed, it was subtracted from the spectrum. The ROI was defined as the area under the peak between the points where the tails went to zero. This ROI represented the net area. The gross area was then defined as the total area under the peak of the original spectrum between the points where the net area tails went to zero.

The final method required plotting the spectrums and visually estimating the slope of the background with a ruler. The plots only allowed for estimating the resolution of the peak. The estimated values were within the uncertainty of the spreadsheet values for 80% of the peaks.

Tables 3 thru 8 show the comparison between the results generated by the PHA software and the spreadsheet software from Figures 16 thru 19. The resolution is not addressed in these tables since it will be addressed in a future tables.

In Tables 3 thru 8 the following notation is used. E(n) is the x-ray peak energy of the nth peak. $I_g(n)$ is the gross number of counts in the nth peak. $I_b(n)$ represents the background counts in the nth peak. I(n) is the net counts in the nth peak.

In another section of this chapter, the issue of intensity ratios will be addressed. When comparing the values of the intensities from Reference 9 and those from the PCA software, more than 80% of the intensity ratios were

within 15% of each other. Additionally, the PCA software provided no method for determining the uncertainty from its calculations. Consequently, the values of the intensities used were determined from the spreadsheet method.

Another issue that will be addressed in a later section of this chapter is calculating the PXR linewidth. The measured linewidths of the observed spectra were used. The PCA software was not used as it gave linewidths that were as wide as the base of the peaks they represented. The uncertainties of the hand measurements are probably a more accurate estimate of the uncertainty than the uncertainties of the spreadsheet calculations.

The uncertainty from using Reference 8, is not included in Tables 3 thru 8, as it was indeterminable.

1. Intensity Analysis

A transmission factor of less than unity reduces the x-ray intensity. The physical parameter to describe transmission is L_a, the absorption length in centimeters, which is dependent upon the absorption coefficient, μ. Table 9 is a list of μ and La for the theoretical PXR peak energies. The values of μ in square centimeters per gram were determined using Reference 11. L_a was computed using the following

$$L_a = \frac{1}{\mu\rho}, \tag{18}$$

where ρ = 2.33g/cm3.

The primary interest of this experiment was determining the effects on the higher order PXR at different crystal thicknesses. One way was to examine the relative intensities of the nth order peaks with respect to the first order peak. The intensity, I(n), (as discussed in Reference 5) is

$$I(n) \propto \omega_B(n) L_a \left|1 - e^{-L/L_a}\right| \left|g_r(\omega_B(n))\right|^2, \qquad (19)$$

From equation (19) it is noted that the intensity is proportional to L_a. When L_a was greater than L, the crystal thickness along the particle beam path, with

$$L = t/\sin\theta_B, \qquad (20)$$

then the intensities of the higher order peaks were decreased. The converse is true. If L is greater than La, then the intensities of the higher order peaks will increase. Table 10 compares the values of L and L_a for the PXR data.

The exponential term in equation (19) approaches unity as L_a becomes much greater than L. This accounts for the lack of higher order peaks in the 20 μm spectrums despite counting for two hours in the case of Figure 15 (<111> orientation) and counting in excess of one hour for Figure 14 (<220> orientation).

n	1 (PHA)	2 (PHA)	1 (SS)	2 (SS)
E(n) (keV)	8.176±.035	16.97±.04	8.176±.035	16.97±.04
E(n)/E(1)	1.0	2.076±.013	1.0	2.076±.013
Peak				
$I_g(n)$	255	42	255	42
$I_b(n)$	14	13	16	16
I(n)	241	29	239±16	26±8
I(n)/I(1)	1.0	0.12	1.0	.109±.041
Area				
$I_g(n)$	4986	1132	4946	755
$I_b(n)$	4153	735	736	416
I(n)	833	397	4210±75	339±34
I(n)/I(1)	1.0	0.477	1.0	.81±.010

Table 3. Comparison of PHA and spreadsheet (SS) analysis of data from 44 μm Si <220> orientaion.

n	1 (PHA)	2 (PHA)	1 (SS)	2 (SS)
E(n) (keV)	8.207±.035	17.16±.04	8.207±.035	17.16±.04
E(n)/E(1)	1.0	2.09±.013	1.0	2.09±.013
Peak				
$I_g(n)$	317	73	317	73
$I_b(n)$	18	16	19	19
I(n)	299	57	298±18	54±10
I(n)/I(1)	1.0	0.19	1.0	0.18±.04
Area				
$I_g(n)$	6054	1592	6035	1723
$I_b(n)$	765	735	834	775
I(n)	5289	857	5201±83	948±50
I(n)/I(1)	1.0	0.16	1.0	0.182±.013

Table 4. Comparison of PHA and spreadsheet (SS) analysis of data from 320 μm Si <220> orientation.

n	1	3	4
E(n) (keV)	4.563±.035	15.301±.04	20.80±.04
E(n)/E(1)	1.0	3.355±.033	4.559±.043
Peak			
$I_g(n)$	683	102	66
$I_b(n)$	65	50	45
I(n)	618	52	21
I(n)/I(1)	1.0	0.084	0.034
Area			
$I_g(n)$	15630	3334	2612
$I_b(n)$	6174	2842	2352
I(n)	9456	492	260
I(n)/I(1)	1.0	0.052	0.027

Table 5. Results of analysis by PHA of 44 μm Si <111> orientation.

n	1	3	4
E(n) (keV)	4.563±.035	15.301±.04	20.80±.04
E(n)/E(1)	1.0	3.355±.033	4.559±.043
Peak			
$I_g(n)$	683	102	66
$I_b(n)$	74	54	45
I(n)	609±28	48±12	21±11
I(n)/I(1)	1.0	0.078±0.02	0.034±0.02
Area			
$I_g(n)$	16812	2611	1866
$I_b(n)$	4354	1921	1484
I(n)	12458±145	690±67	382±20
I(n)/I(1)	1.0	0.055±0.006	0.031±0.005

Table 6. Results of analysis by spreadsheet of 44 μm Si <111> orientation.

n	1	3	4
E(n) (keV)	4.720±.035	15.62±.04	21.15±.04
E(n)/E(1)	1.0	3.31±.032	4.481±.041
Peak		—	
$I_g(n)$	247	103	81
$I_b(n)$	40	28	25
I(n)	207	75	56
I(n)/I(1)	1.0	0.362	0.27
Area			
$I_g(n)$	6648	3200	2516
$I_b(n)$	2915	1855	1431
I(n)	3733	1345	1085
I(n)/I(1)	1.0	0.36	0.29

Table 7. Results of analysis by PHA of 320 μm Si <111> orientation.

n	1	3	4
E(n) (keV)	4.720±.035	15.62±.04	21.15±.04
E(n)/E(1)	1.0	3.31±.032	4.481±.041
Peak			
$I_g(n)$	247	103	81
$I_b(n)$	44	33	28
I(n)	203±17	70±12	53±10
I(n)/I(1)	1.0	0.34±0.09	0.26±0.07
Area			
$I_g(n)$	6440	2834	2301
$I_b(n)$	2156	1489	1288
I(n)	4284±93	1345±66	1013±60
I(n)/I(1)	1.0	0.31±0.02	0.24±0.02

Table 8. Results of analysis by spreadsheet of 320 μm Si <111> orientation.

Using equation (19), Table 11 was created to show how a change in x-ray peak energy can affect the intensity of

<hkl>	E (keV)	μ (cm2/g)	μρ (cm-1)	La (μm)
<220>	8.443	54.6	127.22	78.6
<440>	16.89	7.0	16.31	613.1
<111>	5.171	222	517.3	19.33
<333>	15.51	9.03	21.04	475.3
<444>	20.68	3.83	8.92	1120.6

Table 9. Values of μ and La for theoretical parametric x-ray energy peaks.

<hkl>	E (keV)	t (μm)	μ(cm2/g)	L (μm)	La (μm)
<220>	8.63	20	51.12	52.3	83.93
<220>	8.17	44	60.1	115	71.41
<440>	16.97		6.9	115	622.0
<220>	8.21	320	59.3	836	72.38
<440>	17.16		6.67	836	643.5
<111>	5.19	20	220	52.3	19.51
<111>	4.56	44	315	115	13.62
<333>	15.31		9.39	115	457.1
<444>	20.80		3.77	115	1138.4
<111>	4.72	320	286	836	15.0
<333>	15.62		8.84	836	485.5
<444>	21.15		3.58	836	1198.8

Table 10. Comparison of L and La.

the x-ray peak. The values listed our for a 20 μm crystal and a 44 μm crsytal. Table 11 reveals at low energies

$L_a\left[1 - e^{-L/L_a}\right]$ can change as much as 5% while at higher energies it changes by only 0.1%

<hkl>	E (keV)	t (μm)	L_a (μm)	$L_a\left[1 - e^{-L/L_a}\right]$
<220>	8.17	20	71.41	37.08
<220>	8.63	20	83.93	38.92
<111>	20.68	44	1120.6	109.30
<111>	20.8	44	1138.4	109.42

Table 11. Example calculations of the effects on theabsorption factor in equation (19).

Once the x-ray photons were generated, they passed through several media. The first was a one mil Kapton window (with a window diameter of one inch). Next the photons passed through a three centimeter air gap. Finally, x-rays entered the Si(Li) detector via a two mil berrylium window. Tables 12 thru 14 list the attenuation coefficients for the PXR peak energies. Also found in these tables is the value of the absorption coefficient times the thickness of the media transitted, μρx. Table 15 provides the attenuation factors of the Kapton window, the berrylium window and the air gap.

Knowing the attenuation coefficient, the next step was to determine the intensity of the PXR prior to being transmitted throught the Kapton window.

<hkl>	E (keV)	t (μm)	μ (cm2/g)	μρx
<220>	8.17	44	5.78±.08	.020 5±.0041
<440>	16.97		.773±.004	.0027±.0005
<220>	8.21	320	5.70±.08	.0202±.0041
<440>	17.16		.753±.004	.0027±.0005
<111>	4.56	44	33.8±.8	.120±.024
<333>	15.31		.991±.005	.0035±.0007
<444>	20.80		.501±.002	.0018±.0004
<111>	4.72	320	30.4±.8	.108±.022
<333>	15.62		.943±.005	.0033±.0007
<444>	21.15		.486±.002	.0017±.0003

Table 12. Attenuation coefficient for Kapton ($C_{22}O_5N_2H_{10}$) with ρ = 1.42 g/cm3 and x=0.0025 ± .0005cm.

<hkl>	E (keV)	t (μm)	μ (cm2/g)	μρx[12]
<220>	8.17	44	1.06±.02	.0096
<440>	16.97		.263±.001	.0024
<220>	8.21	320	1.05±.02	.0096
<440>	17.16		.260±.001	.0024
<111>	4.56	44	5.77±.12	.0525±.0063
<333>	15.31		.299±.001	.0027
<444>	20.80		.218±.001	.0002
<111>	4.72	320	5.21±.12	.0474±.0057
<333>	15.62		.291±.001	.0026
<444>	21.15		.216±.001	.0002

Table 13. Attenuation coefficient for berrylium. ρ = 1.82g/cm3 and x = .0050cm.

[12]Uncertainty was less than 2% except where noted.

Using the following equation

$$I(n) = I_0(n)\exp(-\mu\rho x)_{tot}, \quad (21)$$

where

$$(\mu\rho x)_{tot} = \Sigma(\mu\rho x). \quad (22)$$

$I_0(n)$ is the intensity of the PXR after being created and

<hkl>	E (keV)	t (μm)	μ (cm2/g)	μρx
<220>	8.17	44	9.32±.12	.0362±.0061
<440>	16.97		1.17±.01	.0045±.0008
<220>	8.21	320	9.19±.12	.0357±.006
<440>	17.16		1.13±.01	.0044±.0007
<111>	4.56	44	53.0±1.2	.206±.034
<333>	15.31		1.53±.01	.006±.001
<444>	20.80		.711±.003	.0028±.0005
<111>	4.72	320	47.8±1.2	.186±.031
<333>	15.62		1.45±.01	.006±.001
<444>	21.15		.685±.003	.0027±.0005

Table 14. Attenuation coefficient for air. $\rho = 0.001294$ $x = 3.0\pm0.5$cm.

prior to exiting the scattering chamber. I(n) is the detector intensity. Rearranging the terms in equation (21) and solving for $I_0(n)$, equation (21) becomes

$$I_0(n) = I(n)\exp(\mu\rho x)_{tot}. \quad (23)$$

Table 16 is a compilation of the $(\mu\rho x)_{tot}$ values. Figure 20 is a plot of the attenuation factors of the Kapton window, the air gap, the beryllium window, and the product of the three attenuation factors versus x-ray peak energy.

In Table 16, the final column lists the attenuation factors of the various peak energies. Not considered when

determining the factors was the efficiency of the Si(Li) detector. To determine the efficiency, the x-ray peak energy must be known. The peak energy determines whether the Be window or the detector thickness dominate to determine detector efficiency. For x-rays with peak energies below approximately 18 keV, only the beryllium attenuation factor is considered. For energies above 18 keV, the detector thickness is the only contributing factor as the attenuation factor of the Be window is unity.[Ref. 10] Figure 21 is reproduced from Reference 10, and is a plot of detector efficiency versus x-ray energy.

The values in Table 16 for the total attenuation factor can be used to determine the detection efficiency except for the case of the <444> orientations. For the <444> orientations, Figure 10, must be included to account for the detector thickness contribution to the efficiency. For these higher energy x-rays, the total attenuation factors in Table 16 would change from 0.995 to 0.945--approximately a 5% difference. The corrected peak and area intensities are found in Tables 17 and 18. In the x-ray energy range examined, the detector has little bearing on the results; however, in ongoing experiments where PXR above 25 keV are being observed, the detector thickness can reduce the counting efficiency rapidly.[Ref. 10]

<hkl>	t (μm)	$e^{-\mu\rho x}$ (Kapton)	$e^{-\mu\rho x}$ (air gap)	$e^{-\mu\rho x}$ (berrylium)
<220>	44	0.980	0.964	0.990
<440>		0.997	0.996	0.998
<220>	320	0.980	0.965	0.990
<440>		0.997	0.996	0.998
<111>	44	0.887	0.814	0.949
<333>		0.997	0.994	0.997
<444>		0.998	0.997	1.000
<111>	320	0.898	0.830	0.954
<333>		0.997	0.994	0.997
<444>		0.998	0.997	1.000

Table 15. This table lists the attenuation factors for the x-rays going through the Kapton window, the air gap and the berrylium window. The differences in the <111> values of both crystal thicknesses is due to the energy differences between the two n=1 peaks.

<hkl>	E (keV)	t (μm)	$(\mu\rho x)_{tot}$	$e^{-(\mu\rho x)tot}$
<220>	8.17	44	.0661±.017	.936
<440>	16.97		.0096±.0025	.990
<220>	8.21	320	.0660±.017	.936
<440>	17.16		.0095±.0025	.990
<111>	4.56	44	.38±.11	.684
<333>	15.31		.012±.003	.988
<444>	20.80		.0048±.0012	.995
<111>	4.72	320	.34±.10	.712
<333>	15.62		.012±.003	.988
<444>	21.15		.0046±.0012	.995

Table 16. Total attenuation coefficient required for computing $I_0(n)$.

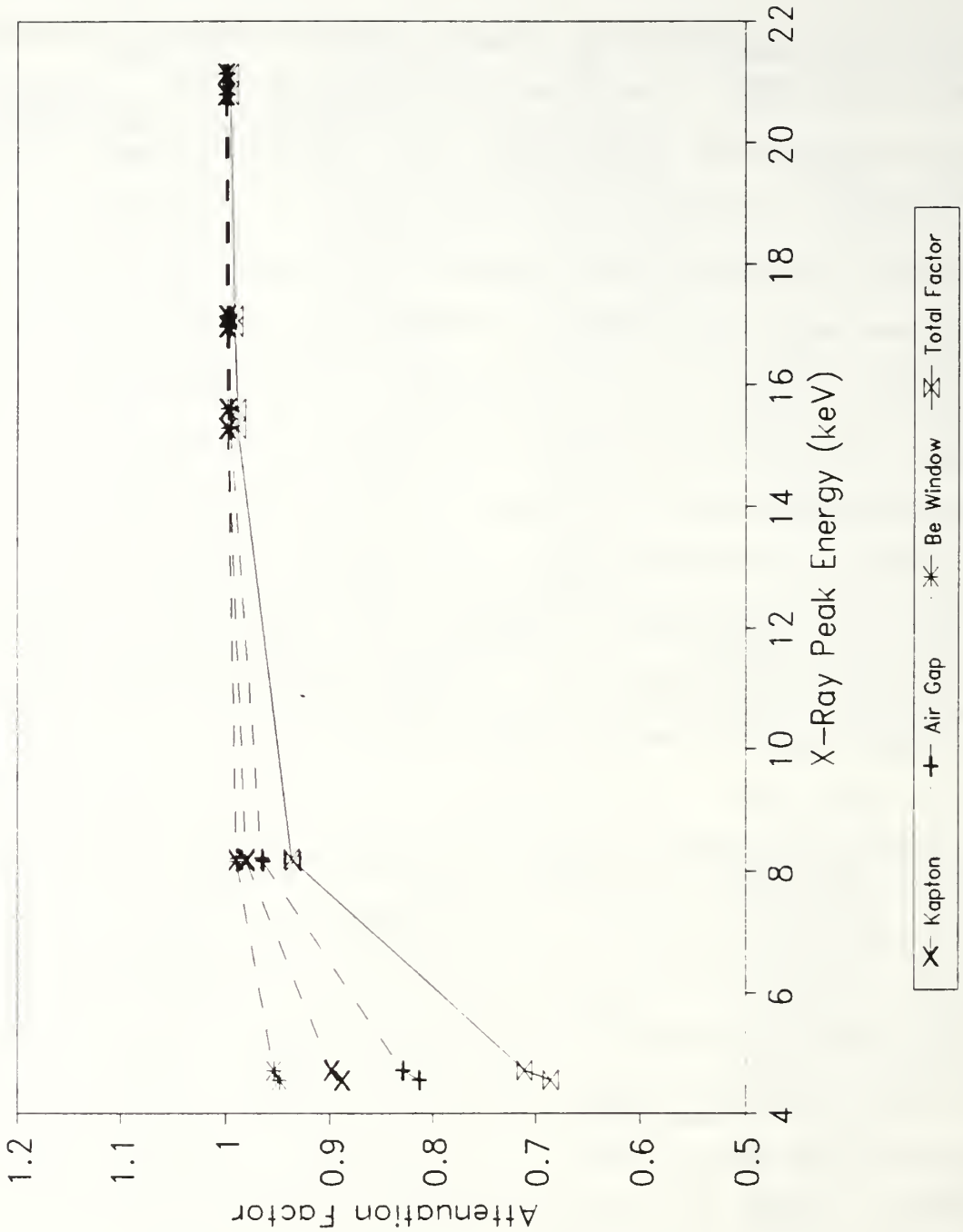

Figure 20. Plot of attenuation factor for the Kapton window, the air gap, the Be window, and the product of the attenuation factors.

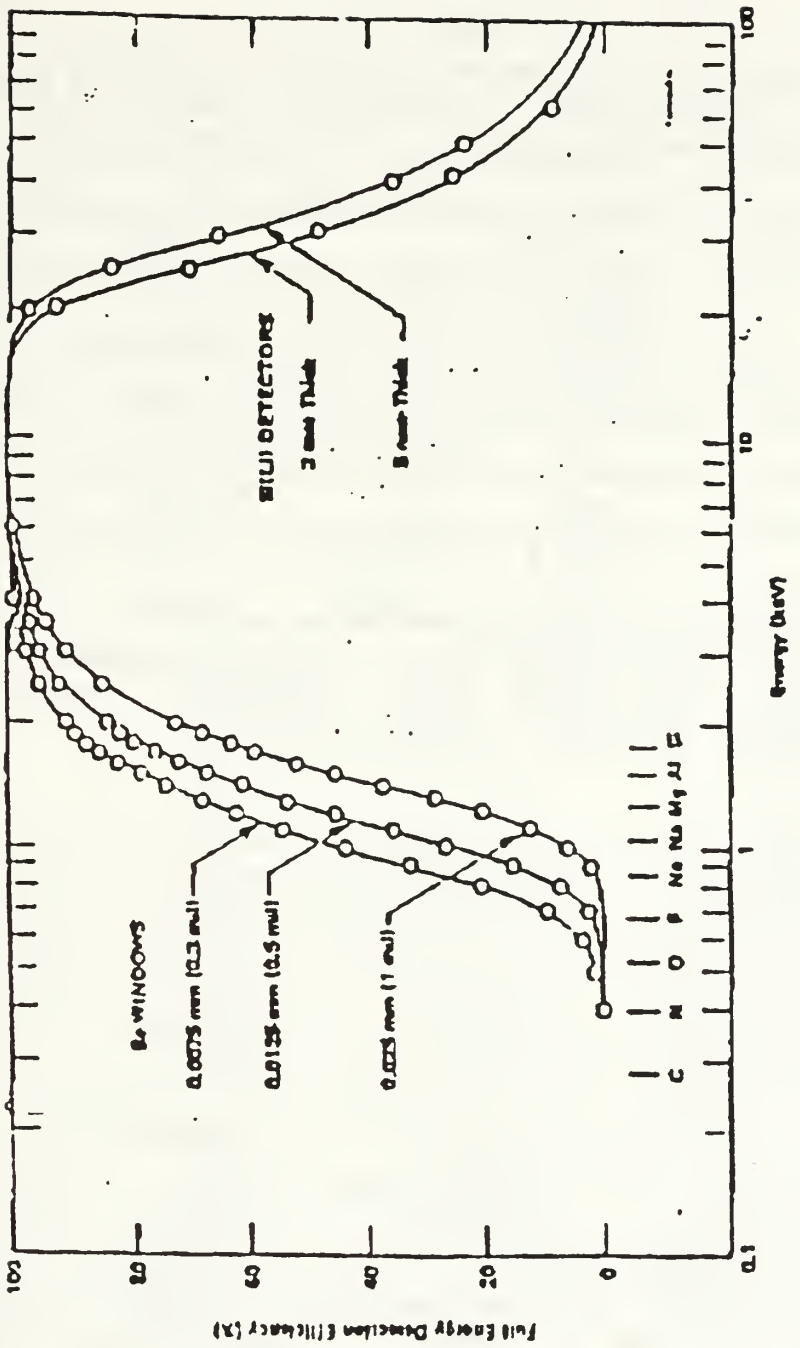

Figure 21. Calculated Full Energy Detection Efficiency Curve for Si(Li) X-Ray Detector. Loss in efficiency at high energies is due to detector thickness. At low energies only attenuation due to the beryllium window is considered.[Ref. 10]

<hkl>	t (μm)	I(n)	I(n)/I(1)	$I_0(n)$	$I_0(n)/I_0(1)$
<220>	44	239±16	1.0	255±18	1.0
<440>		26±8	.109±.041	26±8	.10±.04
<220>	320	219±18	1.0	318±20	1.0
<440>		54±10	.18±.04	55±10	.17±.04
<111>	44	609±28	1.0	889±105	1.0
<333>		48±12	.078±.020	49±12	.06±.02
<444>		21±11	.034±.020	22±11	.025±.015
<111>	320	203±17	1.0	286±37	1.0
<333>		70±12	.34±.09	71±12	.25±.07
<444>		53±10	.26±.07	56±10	.20±.06

Table 17. Comparison of the uncorrected peak intensities and peak intensity ratios with the corrected peak intensities and peak intensity ratios.

<hkl>	I(n)	I(n)/I(1)	$I_0(n)$	$I_0(n)/I_0(1)$
<220>	4210±75	1.0	4498±112	1.0
<440>	339±34	.081±.01	342±34	.076±.009
<220>	5201±83	1.0	5553±130	1.0
<440>	948±50	.182±.013	957±51	.172±.013
<111>	12458±145	1.0	18181±2000	1.0
<333>	690±67	.055±.006	698±68	.038±.008
<444>	382±58	.031±.005	407±58	.022±.005
<111>	4284±93	1.0	6025±610	1.0
<333>	1345±66	.31±.02	1361±67	.23±.03
<444>	1013±60	.24±.02	1079±60	.18±.03

Table 18. Comparison of uncorrected area intensities and area intensity ratios with corrected area intenstites and area intensity ratios.

Tables 19 and 20 are comparisons of the corrected ratios with intensity ratios calculated from the theory. The theoretical ratios were reproduced from Reference 12. Note the discrepancies between the experimental peak ratios and the calculated ratios. The experimental area ratios compare more favorably with the calculated ratios. Figure 22 is a plot of the ratios of the experimental peak ratios to the calculated intensity ratios versus peak number, n. Likewise, Figure 23 is a plot of the ratios of the

<hkl>	$I_0(n)/I_0(1)$ (Calc)	$I_0(n)/I_0(1)$ (exp peak)	(Exp peak) /(calc)
<220>	1.0	1.0	1.0
<440>	.071	.10±.04	1.41 ± .56
<220>	1.0	1.0	1.0
<440>	.19	.17±.04	.89 ± .21
<111>	1.0	1.0	1.0
<333>	.034	.06±.02	1.76 ± .59
<444>	.017	.024±.015	1.41 ± .89
<111>	1.0	1.0	1.0
<333>	.17	.25±.07	1.47 ± .41
<444>	.10	.19±.06	1.9 ± .6

Table 19. Comparison of the corrected peak intensity ratios with theory. Intensities are corrected for attenuation due the Kapton window, the air gap and the Be window.

experimental area ratios to the calculated intensity ratios versus peak number, n.

There was still discussion [Ref. 13] as to whether the calculated ratios were representative of the PXR peak or area intensity ratios. Further investigation is required to determine which case is correct.

2. Resolution Analysis

The secondary purpose of this experiment was to determine how the PXR resolution was affected by the change in PXR peak energy.

<hkl>	$I_0(n)/I_0(1)$ (Calc)	$I_0(n)/I_0(1)$ (exp area)	(Exp area) /(calc)
<220>	1.0	1.0	1.0
<440>	.071	.076±.009	1.07 ± .13
<220>	1.0	1.0	1.0
<440>	.19	.172±.013	.91 ± .07
<111>	1.0	1.0	1.0
<333>	.034	.038±.008	1.12 ± .24
<444>	.017	.021±.005	1.24 ± .29
<111>	1.0	1.0	1.0
<333>	.17	.23±.03	1.35 ± .18
<444>	.10	.17±.03	1.7 ± .3

Table 20. Comparison of the corrected area intensity ratios with theory. Intensities are corrected for attenuation due to the Kapton window, the air gap, and the Be window.

Recall from section **B.** of this chapter, that a straight line approximation was made to estimate the detector resolution (Fig. 8). Estimates of Γ_{det} were made

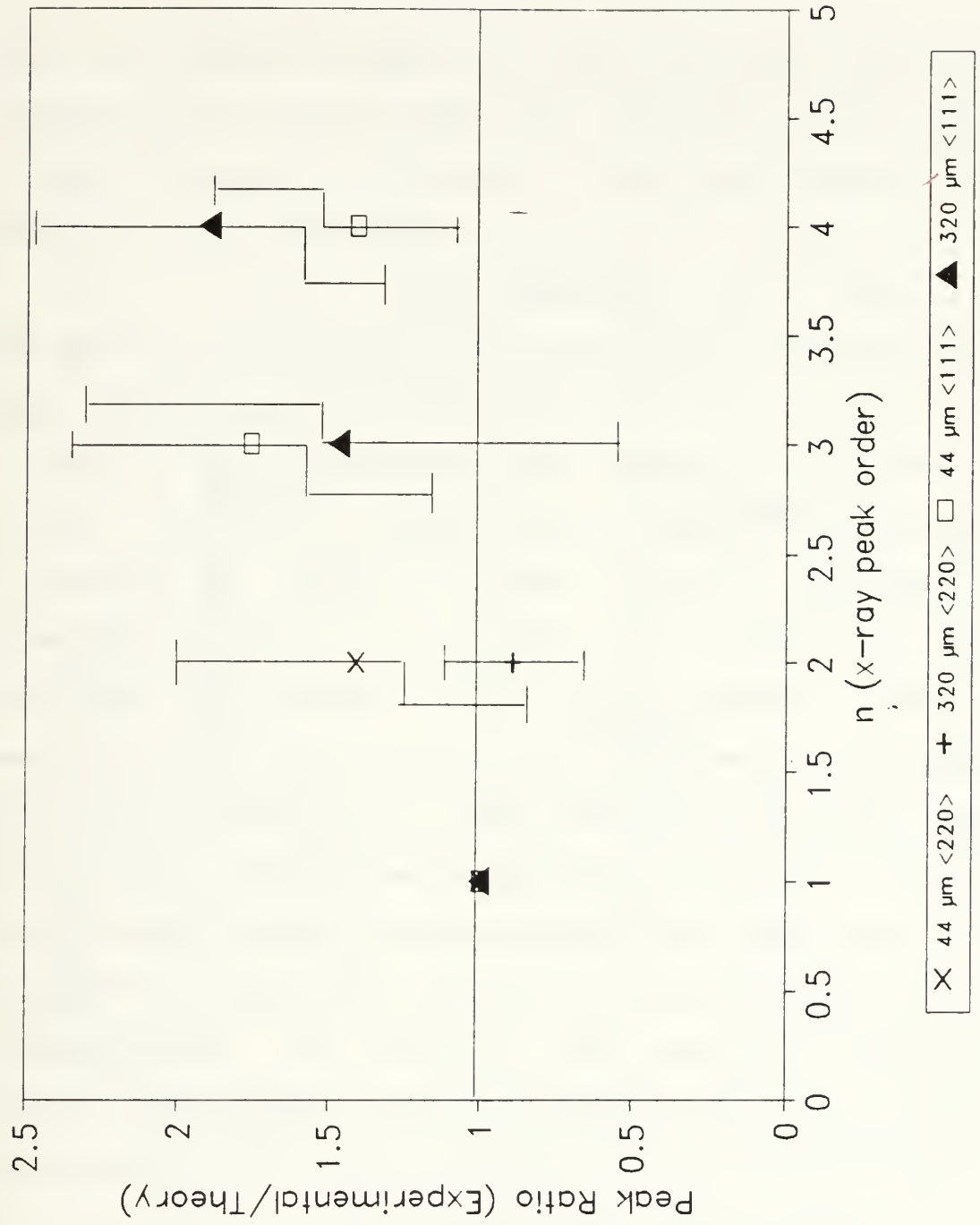

Figure 22. The plot shows a comparison of the experimental ratios divided by the calculated ratios for the peaks versus n, the peak order number. The numerical values are listed in Table 19.

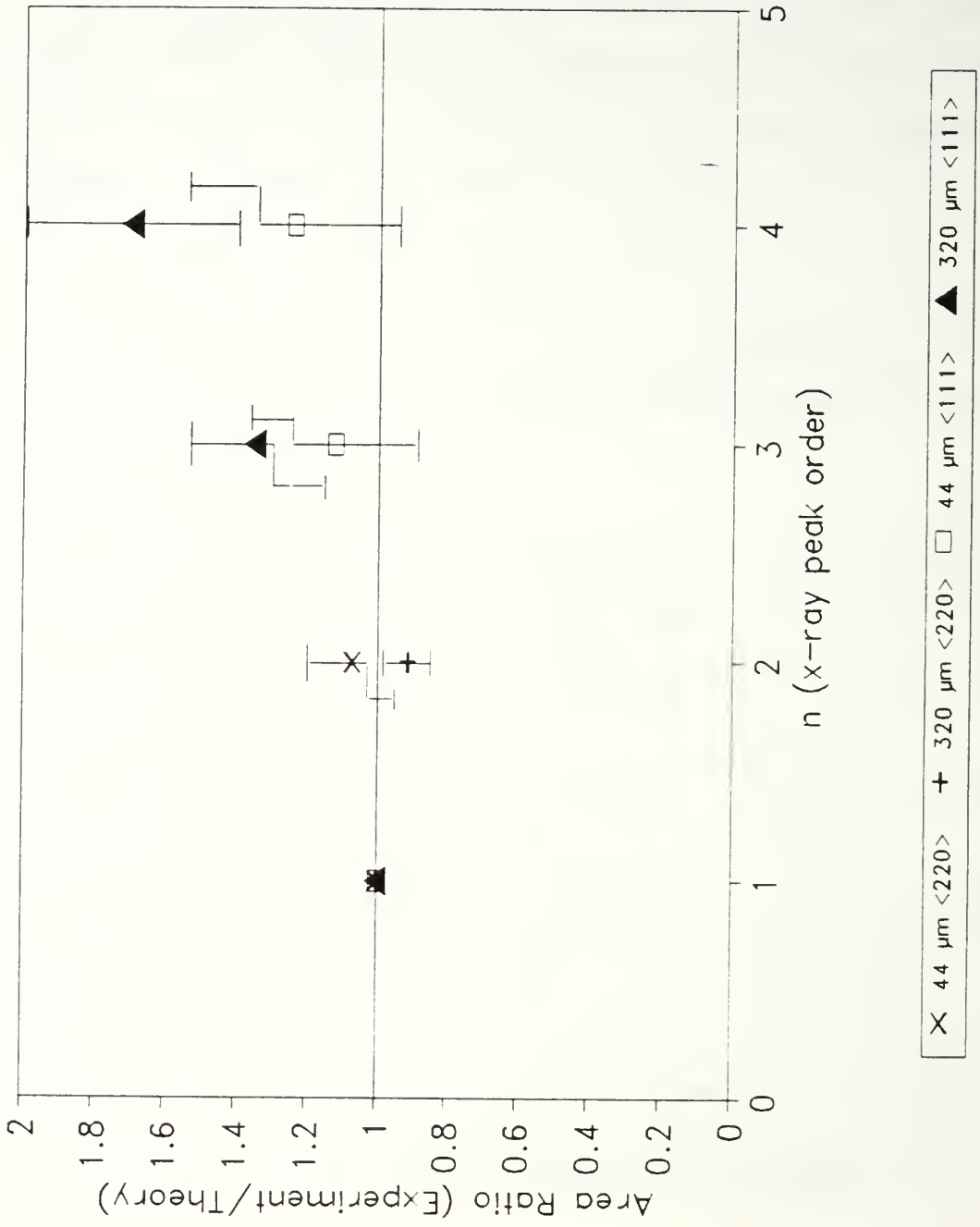

Figure 23. The plot shows a comparison of the experimental ratios divided by the calculated ratios for the areas versus n, the peak order number. The numerical values are listed in Table 20.

and are listed in Table 21. Also in Table 21, are the values Γ_{obs} of each PXR peak, and the derived value, Γ_{PXR}, of each x-ray peak. The latter values were calculated using equation (16) as modified by

$$\Gamma^2_{PXR} = \Gamma^2_{obs} - \Gamma^2_{det} \qquad (24)$$

Table 22 is a comparison of the experimentally determined Γ_{PXR} and the Γ_{PXR} calculated from theory [Ref. 14]. Figures 23 thru 26 are plots of the PXR linewidth versus PXR peak energy. The plots indicate that the linewidth increases as a function of energy. Another point of interest, the linewidths appear to be broaden with increasing crystal thickness for x-rays of the same energy. For each successive peak the value of $\Delta E/E$ decreases as E increases. ΔE is the linewidth of a given peak while E is the energy of the peak. Without more statistics, that is all that can be concluded about the linewidths. The issue as to how parametric x-radiation changes with energy requires further understanding. The starting point must be obtaining a better understanding of the detector and its resolution properties.

<hkl>	E (keV)	t (μm)	Γdet (keV)	Γobs (keV)	ΓPXR (keV)
<220>	8.63	20	0.46±0.05	0.53±0.08	0.26±0.05
<220>	8.17	44	0.46±0.05	0.53±0.08	0.26±0.05
<440>	16.97		0.52±0.04	0.68±0.4	0.44±0.26
<220>	8.21	320	0.46±0.05	0.57±0.03	0.34±0.04
<440>	17.16		0.52±0.04	0.71±0.17	0.48±0.11
<111>	5.19	20	0.44±0.05	0.52±0.08	0.27±0.05
<111>	4.56	44	0.43±0.05	0.51±0.08	0.27±0.05
<333>	15.31		0.51±0.04	0.66±0.4	0.42±0.26
<444>	20.80		0.55±0.05	0.88±0.88	0.69±0.69
<111>	4.72	320	0.44±0.05	0.6±0.1	0.41±0.09
<333>	15.62		0.51±0.04	0.8±0.1	0.61±0.09
<444>	21.15		0.55±0.05	0.9±0.1	0.72±0.10

Table 21. This table is a list of the estimated detector linewidths and the PXR linewidths computed using Γdet.

<hkl>	E (keV)	t (μm)	ΓPXR(exp) (keV)	ΓPXR(calc) (keV)
<220>	8.63	20	0.26±0.05	0.81
<220>	8.17	44	0.26±0.05	0.81
<440>	16.97		0.44±0.26	1.64
<220>	8.21	320	0.34±0.04	0.81
<440>	17.16		0.48±0.11	1.68
<111>	5.19	20	0.27±0.05	0.46
<111>	4.56	44	0.27±0.05	0.46
<333>	15.31		0.42±0.26	1.48
<444>	20.80		0.69±0.69	*
<111>	4.72	320	0.41±0.09	0.49
<333>	15.62		0.61±0.09	1.5
<444>	21.15		0.72±0.10	*

Table 22. Comparison of the experimentally determined PXR linewidths with the theoretically determined PXR linewidths from Reference 14.

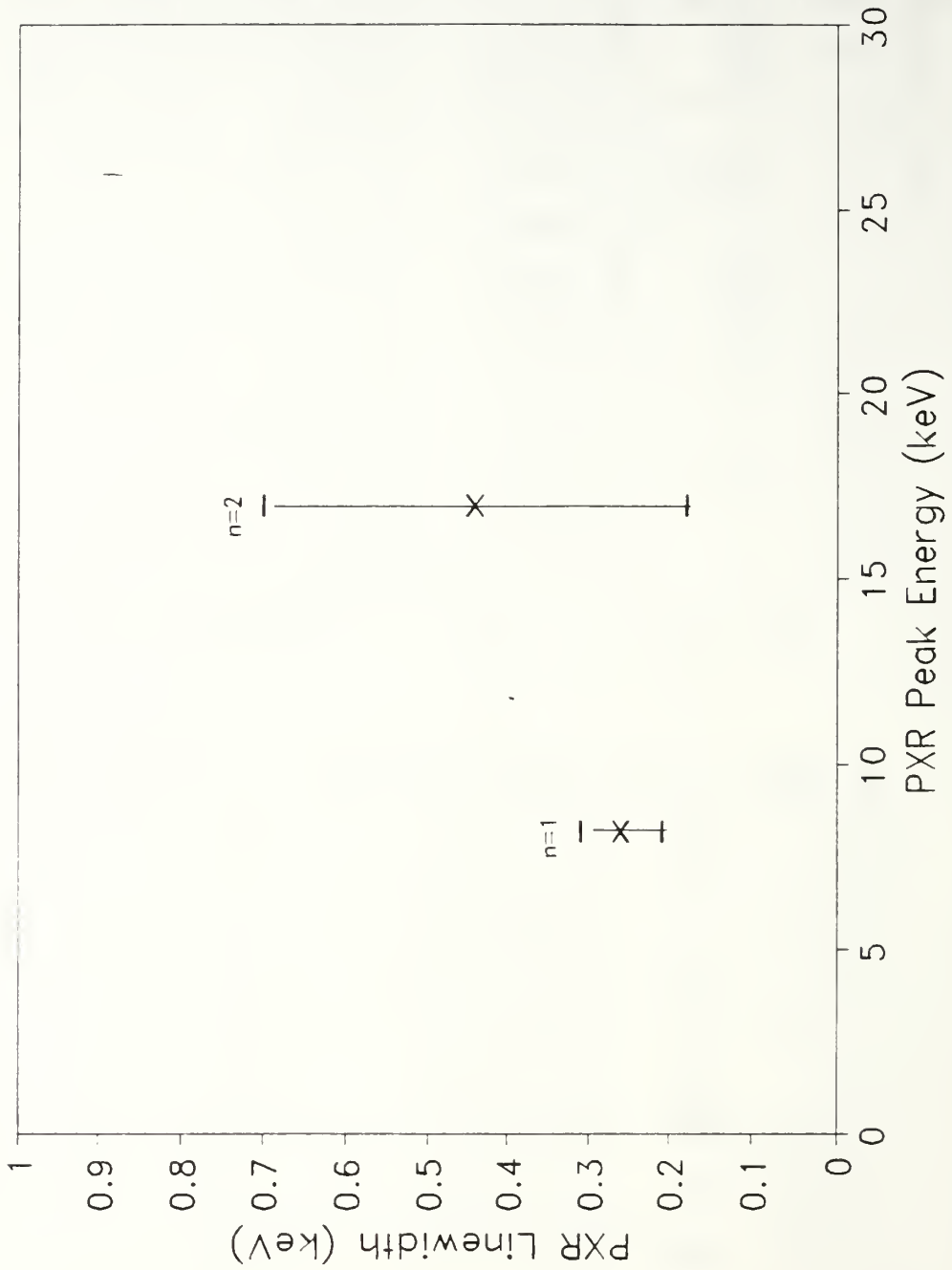

Figure 24. PXR linewidth (keV) versus PXR peak energy for 44 μm <220> orientation. The slope m = 0.0193 with an intercept b = .112 keV.

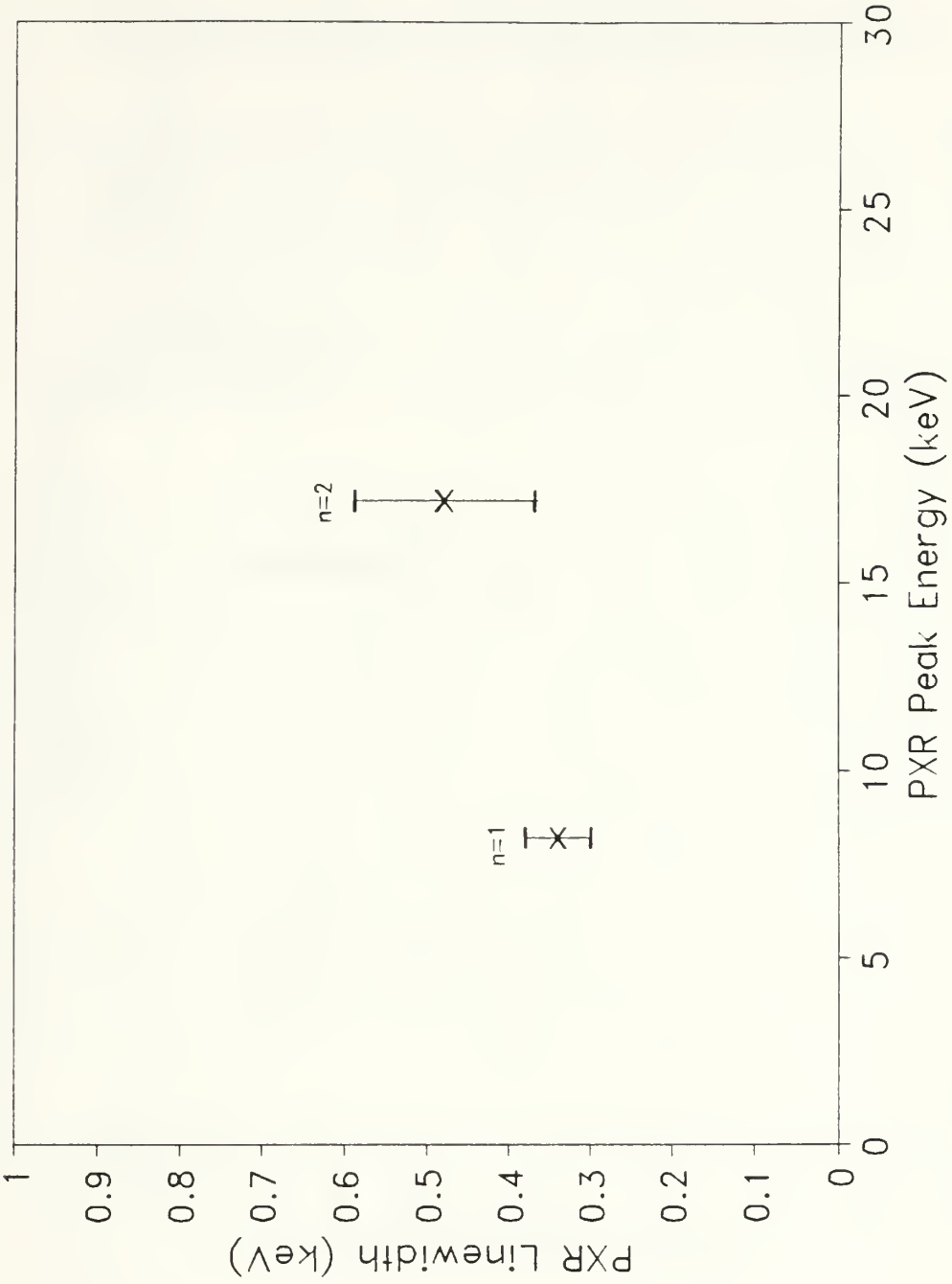

Figure 25. PXR linewidth versus PXR peak energy for the 320 μm <220> orientation. The slope is m = 0.0156 and the intercept is b = 0.212 keV.

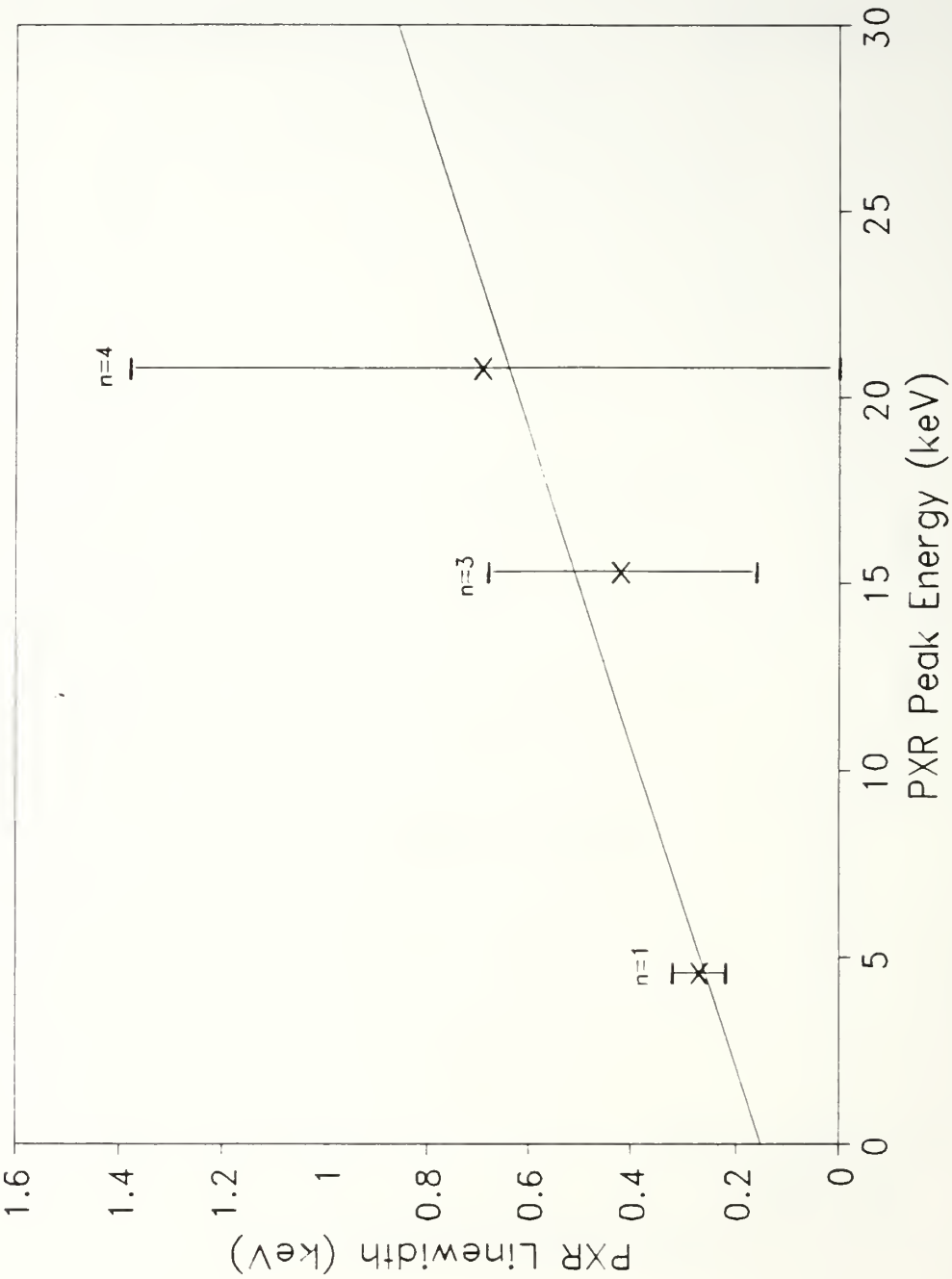

Figure 26. PXR linewidth versus PXR peak energy for the 44 μm <111> orientation. The slope is m = 0.0242, the intercept is b = 0.1316 keV, and the correlation r = 0.9401.

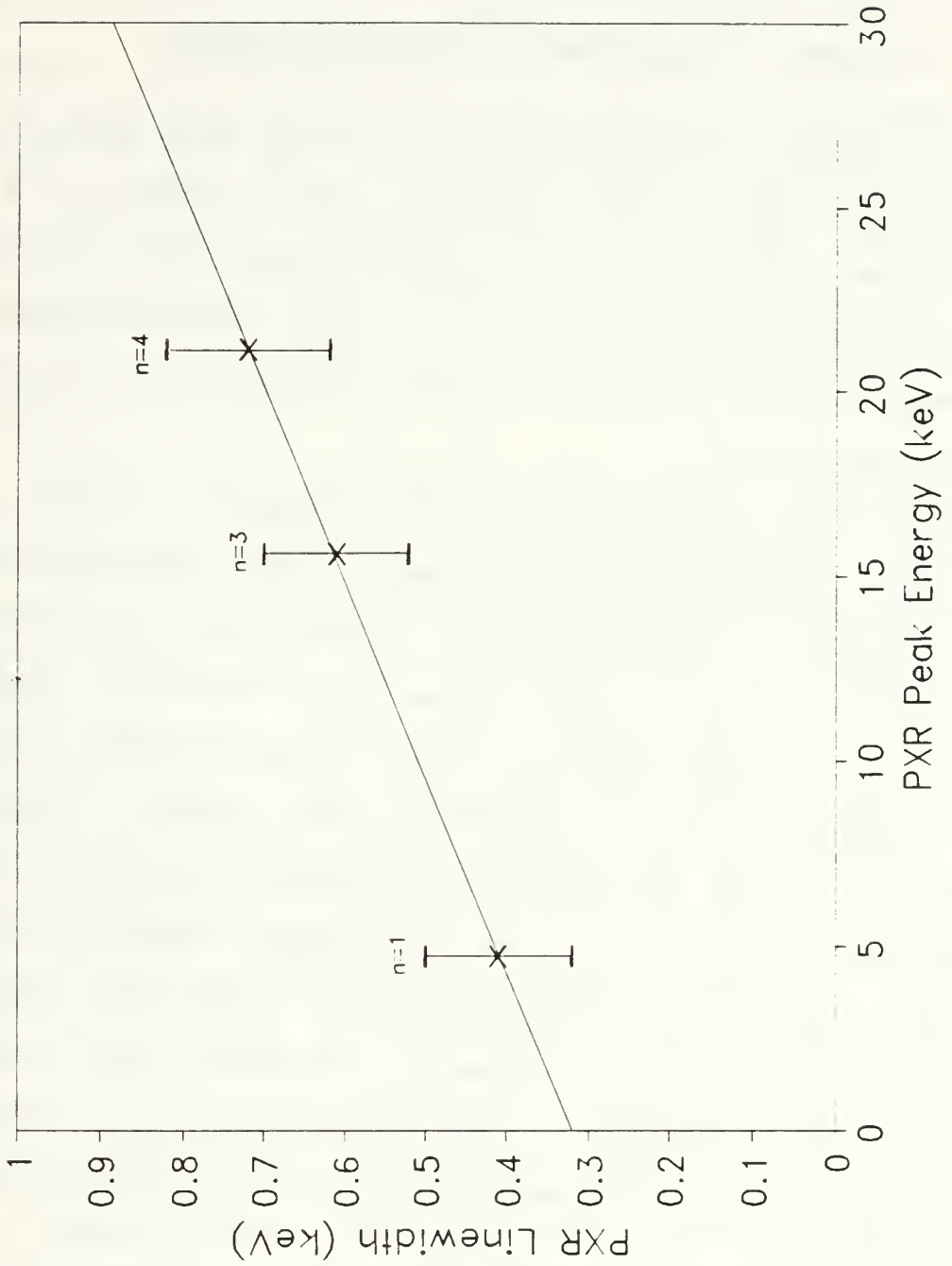

Figure 27. PXR linewidth versus PXR peak energy for the 320 μm <111> orientation. The slope is m = 0.0188, the intercept is b = 0.320 keV, and the correlation is r = 0.9998.

IV. CONCLUSIONS AND RECOMMENDATIONS.

The purpose of this experiment was to study parametric x-radiation from silicon crystals. PXR to order n=4 from silicon were observed. Enhancement of the PXR from higher orders was determined to be due to the crystal thickness. The measurements required careful consideration of several experimental factors.

First, an energy calibration was required to determine the values of the x-ray energy peaks. The calibration was also important in determining the resolution of the x-rays. The resolution of the PXR did not agree with the theory. However, the disagreement may be due to the assumptions made when determining the linewidths of the detector. Another explanation may be the method of calculating the theoretical linewidths. They were calculated without considering the detector apperature or the pipe that the x-ray pass through. These factors need to be reviewed to determine their affects on the x-ray linewidths. In future experiments, energy calibrations must be conducted prior to or following a data collection run.

The second point was ensuring the angular position of the crystal was correct. The Bragg angle of 22.5° was the designated Bragg angle for the experiment. For the 20 μm crystal, this angle led to x-rays with peak energies that

concurred with theory. As for the 44 μm and 320 μm crystals, the Bragg angle for the <220> orientation was 21.5° while the Bragg angle for the <111> orientation was 21.46°. These angles produced bright x-rays at energies that were within ten percent of theory. Thus, despite the small angular deviations from the original Bragg angle, PXR was still observed and there is no other explanation for the x-rays.

Finally, the intensity ratios were determined and compared with the theoretical intensity ratios. The peak intensity ratios deviated from the area intensity ratios by between 2% and 60%. The area ratio intensities concurred better with the calculated ratios than did the peak intensity ratios. Yet, the area ratios only agreed for the <220> orientation of the 44 μm and 320 μm crystals. The <111> orientation differed by 12% to 24% for the 44 m cyrstal and from 35% to 70% for the 320 crystal. More data must be collected to determine if the correct intensity ratio to use is the peak ratio or the area ratio. From the results, preliminary indications suggest the area ratios are the correct ratios. The additional data is needed to also determine the effects on the intensity ratios when changing the Bragg angle by small increments.

Having demonstrated the ability to produce low energy monochromatic x-rays, from a relatively small and low energy

machine, the next phase will be to work on methods to apply the x-rays to real world requirements.

Before pursuing that endeavor more research is required into understanding how the resolution of the PXR is affected by the peak x-ray energy. Second, attention must be devoted to the understanding the electronics associated with the experiment and how the final results are influenced by such instruments. Finally, attention must be given to designing a more compatible target support ladder. On several occasions the ladder was a hindrance to the experiment rather than a support frame for the silicon crystal. With further research and investigation these problems will be solved.

PXR is a new and promising field in x-ray generation. In time it will prove to be a reliable and safe way to produce bright x-rays in areas such as medical treatment facilities or small laboratories. PXR should be actively pursued.

LIST OF REFERENCES

1. Adishchev, Yu.N., and others, "Measurements of Parametric X-Rays from Relativistic Electrons in Silicon Crystals," Nuclear Instruments and Methods in Physics Research, v. B21, pp. 49-55, 1987.

2. Rule, D.W., and others, "Production of X-Rays by the Interaction of Charged Particle Beams with Periodic Structures in Crystalline Materials," paper no. 25 presented at SPIE's International Symposium on Optical Science and Engineering Conf. no. 1552 Short Wavelength Radiation Sources, San Diego, California, 21-26 July 1991.

3. Baryshevsky, V.G., and others, "Experimental Observation of Parametric X-Rays from Ultrarelativistic Electrons," J. Physics D: Applied Physics, v. 19, pp. 171-176, 1986.

4. Osborne, M.J.,"Higher Order Parametric X-Rays," Master's Thesis, Naval Postgraduate School, Monterey, California, December 1991.

5. Faranchuk, I.D. and Ivanshin, A.V., "Theoretical Investigation of the Parametric X-Ray Features.," J. Physique, v. T46,no. 11, pp. 1981-1986, November 1985.

6. Experiments in Nuclear Science AN34 Laboratory Manual, 3d ed., Revised, pp. 167-168, EG&G Ortec Incorporated, 1984.

7. Allison, S.K., and Compton, A.H., X-Rays in Theory and Experiment, 2d ed., p. 745, D. Van Nostrand Company, Inc, 1935.

8. Personal Computer Analyzer, The Nucleus® Inc, March 1988.

9. Quattro® Pro, v. 1.0, Borland International, 1989.

10. Adelphi Technology, Inc, Palo Alto, California, Private Communication, A. Ho to Author, Subject: Si(Li) X-Ray Detector Warranted Specifications and Performance, 162049Z APR 92.

11. Berger, M.J., and Hubbell, J.H., XCOM: Photon Cross Section on A Personal Computer, U.S. Department of Commerce, National Bureau of Standards, Gaithersburg, Maryland, 1987.

12. Naval Surface Warfare Command, Silver Spring, Maryland, Private Communication, D. Rule, and R. Fiorito to X. K. Maruyama, Subject: Summary of Comparison Between Experiment and Theory (U), 142356Z NOV 91.

13. Private Communication between D.W. Rule, and R.B. Fiorito, Naval Surface Warfare Command, Silver Spring, Maryland, and the author, April 22, 1992.

14. Piestrup, M.A., "Parametric Radiation as an Intense Monochromatic X-Ray Source," U.S. Department of Energy, Small Business Innovation Research Proposal, p.30, February, 1992.

INITIAL DISTRIBUTION LIST

No. Copies

1. Defense Technical Information Center.....2
   Cameron Station
   Alexandria, VA 22314-6145

2. Library, Code 52.....2
   Naval Postgraduate School
   Monterey, CA 93943-5002

3. Dr. K. E. Woehler, Code Ph/Wh.....1
   Department of Physics
   Naval Postgraduate School
   Monterey, CA 93943-5002

4. Professor X. K. Maruyama, Code Ph/Mx.....4
   Department of Physics
   Naval Postgraduate School
   Monterey, CA 93943-5002

5. Professor J. R. Neighbours, Code Ph/Nb.....1
   Department of Physics
   Naval Postgraduate School
   Monterey, CA 93943-5002

6. LT Scott R. Evertson, USN. 1
   23217 Cuestport Drive
   Valencia, CA 91355

7. Dr. R. B. Fiorito, Code R41.....1
   Naval Surface Warfare Center
   10901 New Hampshire Avenue
   Silver Spring, MD 20903-5000

8. Dr. D. W. Rule, Code R41.....1
   Naval Surface Warfare Center
   10901 New Hampshire Avenue
   Silver Spring, MD 20903-5000

9. Dr. M. A. Piestrup.....1
   2181 Park Blvd.
   Palo Alto, CA 94306

10. Mr. D. Snyder, Code 61PH.....1
    Department of Physics
    Naval Postgraduate School
    Monterey, CA 93943-5002

Thesis
E825 Evertson
c.1 Experimental considerations of higher order parametric x-rays from silicon crystals of varying thicknesses.

Thesis
E825 Evertson
c.1 Experimental considerations of higher order parametric x-rays from silicon crystals of varying thicknesses.

AMERICAN BINDERY 2 9-93

DUDLEY KNOX LIBRARY
3 2768 00034163 0